Improving Tropical Cyclogenesis Forecasts of Hurricane Irma (2017) through the Assimilation of All-Sky Infrared Brightness Temperatures

CHRISTOPHER M. HARTMAN,[a,b] XINGCHAO CHEN,[a,b] AND MAN-YAU CHAN[a,b]

[a] *Department of Meteorology and Atmospheric Science, The Pennsylvania State University, University Park, Pennsylvania*
[b] *Center for Advanced Data Assimilation and Predictability Techniques, The Pennsylvania State University, University Park, Pennsylvania*

(Manuscript received 19 July 2022, in final form 18 November 2022)

ABSTRACT: The assimilation of satellite all-sky infrared (IR) brightness temperatures (BTs) has been shown in previous studies to improve intensity forecasts of tropical cyclones. In this study, we examine whether assimilating all-sky IR BTs can also potentially improve tropical cyclogenesis forecasts by improving the pregenesis cloud and moisture fields. By using an ensemble-based data assimilation system, we show that the assimilation of upper-tropospheric water vapor channel BTs observed by the *Meteosat-10* SEVIRI instrument two days before the formation of a tropical depression improves the genesis forecast of Hurricane Irma (2017), a classic Cape Verde storm, by up to 24 h while also capturing its later rapid intensification in deterministic forecasts. In an experiment that withholds the assimilation of all-sky IR BTs, the assimilation of conventional observations from the Global Telecommunications System (GTS) leads to the premature genesis of Hurricane Irma by at least 24 h. This premature genesis is shown to result from an overestimation of the spatial coverage of deep convection within the African easterly wave (AEW) from which Irma eventually forms. The gross overestimation of deep convection without all-sky IR BTs is accompanied by higher column saturation fraction, stronger low-level convergence, and the earlier spinup of a low-level meso-β-scale vortex within the AEW that ultimately becomes Hurricane Irma. Through its adjustment to the initial moisture and cloud conditions, the assimilation of all-sky IR BTs leads to a more realistic convective evolution in forecasts and ultimately a more realistic timing of genesis.

SIGNIFICANCE STATEMENT: Every year hurricanes impact the lives of thousands of people living along the eastern coast of the United States. Many of these storms originate from tropical disturbances that exit the west coast of Africa. To give the public more warning time ahead of these storms, it is important to improve the forecasts of their formation. This study uses a system developed at The Pennsylvania State University to incorporate satellite observations into forecasts of a classic Cape Verde storm, Hurricane Irma (2017), two days before it formed. By using satellite-collected radiances, we improve the timing of its formation by up to 24 h due to a better representation of the mesoscale tropical disturbance from which it originated.

KEYWORDS: Tropical cyclones; Data assimilation; Numerical weather prediction/forecasting

1. Introduction

The formation of a tropical depression from a preexisting tropical disturbance is an inadequately understood phenomenon. Details of this early stage in the life cycle of a tropical cyclone (TC) (aka, tropical cyclogenesis; hereafter "genesis") have been challenging to uncover and forecast due to 1) difficulties in understanding the complex nonlinear interactions that occur across scales ranging from the convective up to synoptic scales (Emanuel 2018; Tang et al. 2020; Nunez Ocasio 2021), and 2) a lack of in situ observations over the open ocean.

The environmental conditions favorable for genesis have been known for years. Aside from high sea surface temperatures, these conditions include low vertical wind shear, plentiful midlevel moisture, and high vertical instability (Gray 1968; DeMaria et al. 2001). Observational studies have also pointed out that genesis is usually related to a preexisting synoptic-scale tropical disturbance (e.g., Reed et al. 1977; Gray 1968; Briegel and Frank 1997; Ritchie and Holland 1997). For example, the most common synoptic-scale disturbance involved in the genesis of Atlantic TCs is the African easterly wave (AEW)—at least 70% of Atlantic TCs form in association with AEWs (Russell et al. 2017). In short, it is possible to locate approximate preferred regions of genesis based on the large-scale environmental conditions and preexisting synoptic-scale tropical disturbances.

The strong association between AEWs and genesis is particularly interesting. Dunkerton et al. (2009) proposed that genesis preferentially occurs in regions where the lower-tropospheric AEW-relative streamlines exhibit a closed circulation (specifically, the center of this meso-α-scale circulation; also known as the "marsupial pouch," or "pouch" in short). Their reasoning is that the pouch not only provides a region of cyclonic rotation and weak strain/shearing deformation, but also protects the tropical disturbance within it from potentially harmful environmental conditions (e.g., dry air intrusion). This marsupial pouch paradigm has gained traction over the last decade as it has been reinforced by multiple modeling studies (e.g., Wang et al. 2010; Li and Pu 2014; Asaadi et al. 2016, 2017; Rajasree et al.

Supplemental information related to this paper is available at the Journals Online website: https://doi.org/10.1175/MWR-D-22-0196.s1.

Corresponding author: Xingchao Chen, xzc55@psu.edu

DOI: 10.1175/MWR-D-22-0196.1

2016a,b) and field campaigns, including the Tropical Cyclone Structure 2008 field experiment (TCS-08; Montgomery et al. 2010a), the Pre-Depression Investigation of Cloud-systems in the Tropics (PREDICT; Montgomery et al. 2012), and NASA's Genesis and Rapid Intensification Processes field experiment (GRIP; Braun et al. 2013).

Despite our ability to locate probable areas of genesis (i.e., areas along the forecasted AEW track that have favorable large-scale environments), it is still an unmet challenge to accurately forecast whether the genesis will happen and/or the exact genesis timing. This is due to uncertainties in convective-scale processes and their interactions with the large-scale environment. While tropical cyclones appear to form from multiscale interactions between a preexisting synoptic-scale disturbance and convection within the disturbance, it is still not entirely clear how. Ritchie and Holland (1997) and Simpson et al. (1997) proposed that the mesoscale convective vortices (MCVs) in the stratiform region of mesoscale convective systems (MCSs) collectively reinforce the midlevel circulation of the larger-scale disturbance. This midlevel circulation was believed to subsequently lower toward the surface via evaporatively cooled downdrafts, thereby leading to genesis (Bister and Emanuel 1997). In contrast with that "top-down" paradigm, Hendricks et al. (2004) and Montgomery et al. (2006) proposed a "bottom-up" pathway to genesis, whereby the low-level tropical depression vortex is built by the successive merging of convective towers containing strong cyclonic vorticity anomalies that they named "vortical" hot towers (VHTs). This insight was made possible by cloud-resolving simulations and was reinforced by several modeling studies (e.g., Tory et al. 2006a,b; Shin and Smith 2008; Van Sang et al. 2008; Braun et al. 2010). Observational studies around that time (Reasor et al. 2005; Sippel et al. 2006; Houze et al. 2009) also documented the prevalence of VHTs. Since the updrafts of these convective towers dominate the mass flux profile at low-levels, Nolan (2007) and Houze et al. (2009) suggested that VHTs are the dominant player in the formation of the low-level vortex while the stratiform region in MCSs at midlevels plays a supporting role. Regardless of the precise mechanisms by which convection leads to a tropical cyclone, the community's consensus is that convective-scale processes play an important role in genesis.

Given the important role convection plays in the genesis process, it stands to reason that we must adequately capture its evolution in forecasts if we wish to accurately predict the timing of genesis. Over the last decade, studies have investigated potential connections between the temporal evolution of spatial patterns of convection in predepression tropical disturbances and subsequent genesis. Reanalysis-based (Leppert et al. 2013a,b) and observation-based (Zawislak and Zipser 2014) studies have suggested that the convective intensity near the circulation center might be much less of a factor than the convective area in the hours and days leading up to genesis. Wang (2018) stressed the importance of looking at the spatial pattern of convection in genesis studies—they observed that genesis was more likely to occur when convective intensity increased in the inner pouch region but stayed the same or decreased in the outer pouch region in the hours leading up to genesis. The spatial pattern and evolution of multiday convective bursts was analyzed in several recent observational studies (Kerns and Chen 2013; Chang et al. 2017; Bell and Montgomery 2019). These studies indicate that vigorous multiday convective bursts that are conducive to genesis occur in both developing and nondeveloping disturbances. These studies collectively reinforce the notion that the occurrence of genesis has a complicated dependence on pregenesis convection.

Since the convective evolution of pregenesis disturbances is quite complex, the accurate prediction of genesis depends on an accurate representation of it. Since in situ and aircraft observations are sparse over the open ocean, one way to achieve a better representation of convection in forecasts is to assimilate high resolution [>1 pixel $(30\ \text{km})^{-2}$] all-sky infrared (IR) brightness temperatures (BTs). At this point in time, a number of real-data studies have shown the benefits of assimilating all-sky IR BTs in the forecasts of severe thunderstorms (e.g., Zhang et al. 2018, 2021; Sawada et al. 2019; Jones et al. 2020), tropical convection (e.g., Chan et al. 2020; Chan and Chen 2022), and tropical cyclone rapid intensification (e.g., Honda et al. 2018; Minamide and Zhang 2018; F. Zhang et al. 2019; Minamide et al. 2020; Hartman et al. 2021). These studies unanimously found that the assimilation of all-sky IR BTs improved the evolution of clouds in forecasts. It is thus possible that assimilating all-sky IR BTs could improve genesis forecasts.

In this study, we will examine this possibility in the context of Hurricane Irma (2017). This storm was chosen because it is a classic Cape Verde storm that ultimately impacted many areas in the Caribbean and continental United States. In addition, this particular storm formed well before the expectation of the National Hurricane Center's (NHC's) operational guidance (Cangialosi et al. 2018).

This paper is organized as follows. Section 2 provides a brief meteorological history of Irma and section 3 describes the experimental setup and data assimilation (DA) system used. We will then present the results of deterministic forecasts initialized with the DA system in section 4. Finally, the conclusions of this study and avenues of future research are presented in section 5.

2. Brief overview of Hurricane Irma (2017)

Before proceeding, a brief description of Hurricane Irma (2017) is warranted. As a classic Cape Verde storm, Hurricane Irma formed from an AEW that moved into the eastern Atlantic Ocean late in the day on 27 August. On that day, despite favorable environmental conditions, the operational NHC guidance projected no chance of TC development over the next 48 h and a 20% chance of TC development over the next 5 days (Table 1). At 0000 UTC 28 August (48 h before genesis), these probabilities were relatively unchanged even though deep convection persisted within the northern portion of the wave trough (Fig. 1a). Over the next 48 h this deep convection organized (Fig. 1b) faster than anticipated, and by 0000 UTC 30 August (hereafter "genesis time") the NHC classified the resulting convective system as a tropical depression when a well-defined surface circulation was detected.

The track and intensity of Irma after genesis are shown for reference in Figs. 1e and 1f, respectively. After forming roughly 150 miles west of the Cabo Verde Islands, it moved westward into favorable environmental conditions and underwent rapid

TABLE 1. The 48-h and 5-day genesis probabilities from the National Hurricane Center Tropical Weather Outlook (https://www.nhc.noaa.gov/archive/xgtwo/gtwo_archive_list.php?basin=atl). The bold font indicates the 12-h period that is the focus of this study.

		NHC genesis probabilities	
Time	Hours before genesis	48-h	5-day
0600 UTC 27 Aug	66	0%	20%
1200 UTC 27 Aug	60	0%	20%
1800 UTC 27 Aug	**54**	**0%**	**20%**
0000 UTC 28 Aug	**48**	**0%**	**40%**
0600 UTC 28 Aug	**42**	**10%**	**50%**
1200 UTC 28 Aug	36	30%	70%
1800 UTC 28 Aug	30	40%	80%
0000 UTC 30 Aug	0	Genesis	

intensification (RI). Irma became a hurricane within the next 30 h and a major hurricane within 48 h. The cloud fields and lower tropospheric streamlines are shown during RI (Fig. 1c) and at major hurricane stage (Fig. 1d). These subplots illustrate the axisymmetrization of the convection that occurred within the increasingly well-defined low-level vortex during Irma's path to maturity.

This study will focus on improving deterministic forecasts initialized during a 12-h period centered on 48-h pregenesis (bold text in Table 1). This period (from 1800 UTC 27 August to 0500 UTC 28 August) was chosen because the operational NHC guidance called for low probabilities of development over the next 48 h (0%) to 5 days (<50%), which indicates a low practical predictability of genesis during this period. Although the focus of this study is on genesis, we will also examine the impacts of assimilating all-sky IR BTs on the later RI of Irma.

3. Methodology

This section describes the DA system and forecast model used, the experimental design, and the observations assimilated.

a. DA and forecast system

The DA system we used for this study is the Pennsylvania State University ensemble Kalman filter (PSU WRF-EnKF) system. This system converts observations into model state variable updates using the ensemble square root filter of Whitaker and Hamill (2002). The ensemble is then integrated to the next

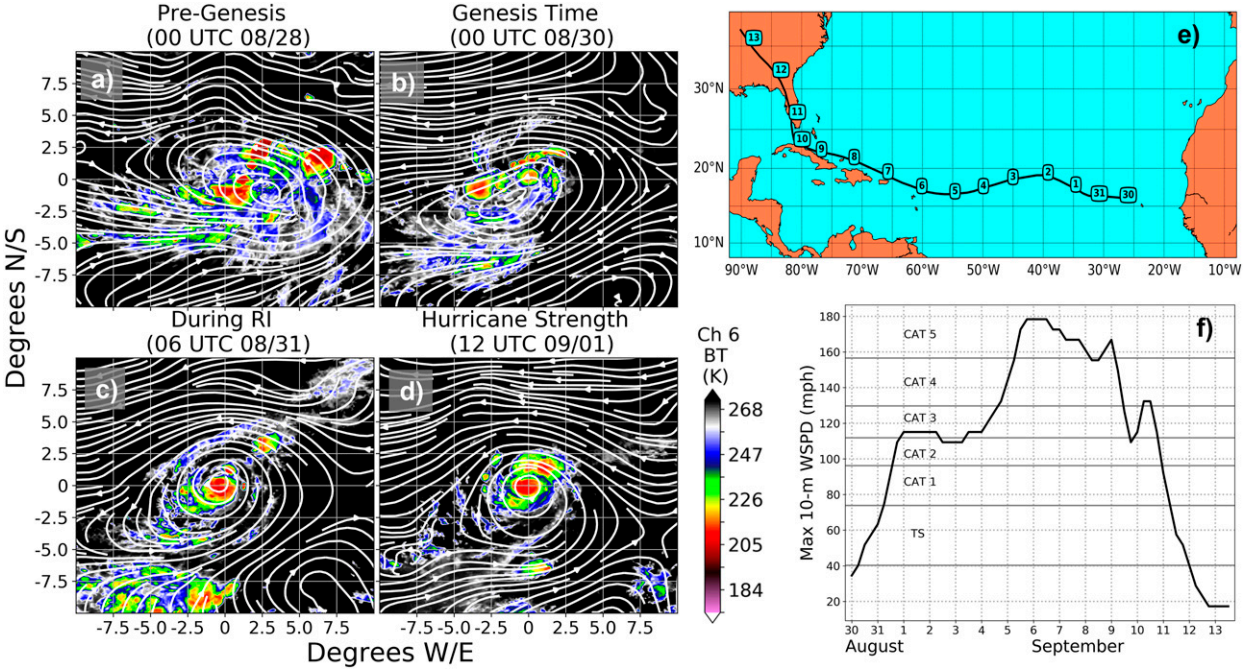

FIG. 1. *Meteosat-10* channel-6 BT overlaid with ERA5 850-hPa streamlines of Irma (a) 48-h pregenesis (0000 UTC 28 Aug), (b) at genesis time (0000 UTC 30 Aug), (c) during rapid intensification (0600 UTC 31 Aug), and (d) at major hurricane strength (1200 UTC 1 Sep). Also shown are the (e) track and (f) maximum 10-m wind speed of Irma from the National Hurricane Center HURDAT2 database starting from genesis time. Note that for this study we define genesis time (0000 UTC 30 Aug) as the first occurrence of a tropical depression in the HURDAT2 database. Numbers within rounded squares in (e) represent the day of the month.

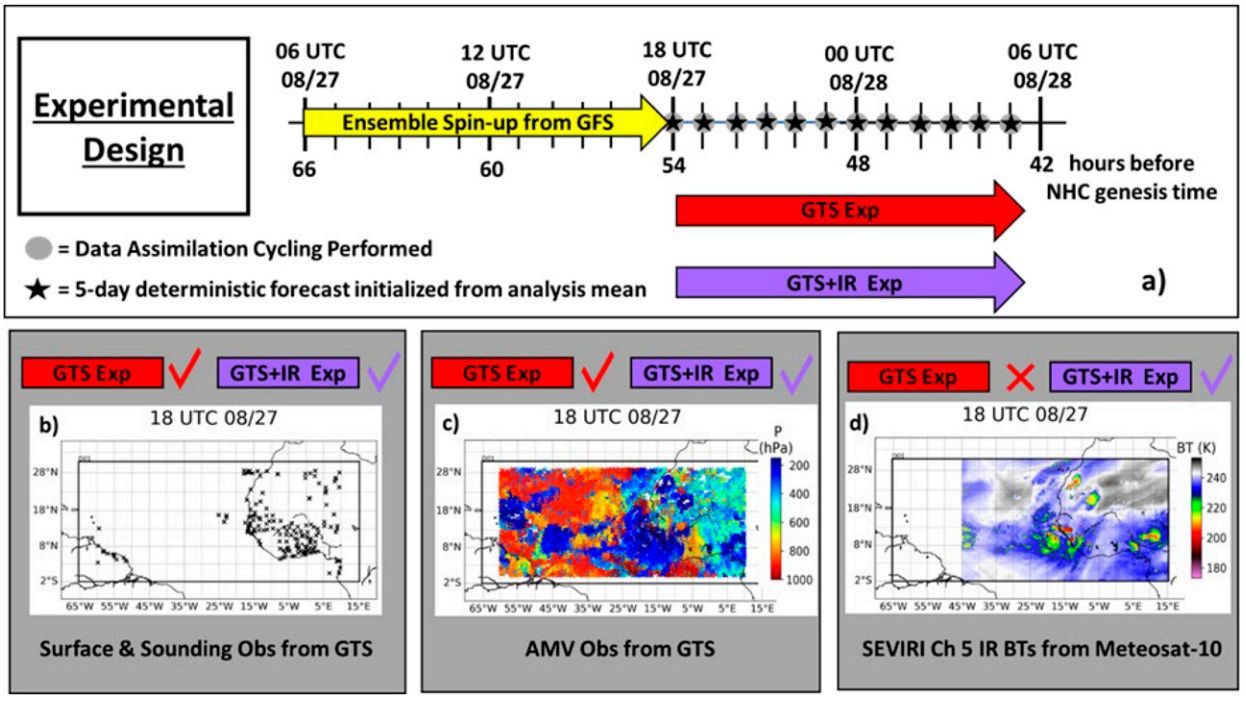

FIG. 2. (a) Overview of the experimental design including (b)–(d) the locations of each type of observation assimilated during the first data assimilation cycle. See text for more details.

DA analysis time point using the Advanced Research version of the Weather Research and Forecasting (WRF) Model version 3.6.1 (Skamarock et al. 2008). The PSU WRF-EnKF system has been used for real-data case studies since 2008 (Meng and Zhang 2008). For ease of parallelization, it performs DA in a joint state-observation space (Tarantola 1987; Anderson 2001) using the high latency parallel implementation of Anderson and Collins (2007). A total of 60 ensemble members were used in this study and 80% relaxation to prior perturbations (Zhang et al. 2004) was applied to avoid filter divergence. Finally, the Community Radiative Transfer Model (CRTM; Han et al. 2006, 2007; Weng 2007) version 2.1.3 served as the observation operator when assimilating all-sky IR BTs.

Throughout this study, the WRF Model was applied on a single stationary domain with a 9-km horizontal grid spacing over the area indicated by the black rectangle in Fig. 2b. This domain size (865 grid points in the east–west direction and 371 grid points in the north–south direction) was chosen to ensure that it was large enough to contain both the storm and its parent AEW, and to reduce the potential impacts of boundary effects. The 9-km spacing was chosen as a compromise between the model domain size and horizontal resolution. In the vertical, there were 43 model levels extending to 10 hPa. Parameterization schemes used include: the Thompson double-moment microphysics scheme (Thompson et al. 2008), the Yonsei University planetary boundary layer scheme (Hong et al. 2006), and the Rapid Radiative Transfer Model (RRTM) longwave and shortwave radiation schemes (Iacono et al. 2008). Finally, surface fluxes of momentum, as well as sensible and latent heat, were parameterized following Green and Zhang (2013).

No cumulus parameterization scheme was used in this study. While the 9-km grid spacing used here cannot well resolve individual convective cells, previous studies have shown that such a gray-zone grid spacing is capable of resolving MCSs and TCs without using a cumulus parameterization scheme (e.g., He et al. 2019; Wang et al. 2015; Ying and Zhang 2018; Zhang et al. 2017; Chen et al. 2018a,b; Chen and Zhang 2019; Ying and Zhang 2017; Chan et al. 2020; Ou et al. 2020; Chen et al. 2021a,b; Chan and Chen 2022; Chen et al. 2022a,b). Recent studies also indicate that regional simulations using such a grid spacing can capture the primary physical processes related to TC genesis (e.g., Montgomery et al. 2010b) and MCS energetics (e.g., Chen et al. 2021a).

b. *Experimental design*

A brief overview of the experimental design is provided in Fig. 2a. Beginning at 66-h pregenesis (0600 UTC 27 August), a 60-member ensemble was created by adding perturbations to the National Centers for Environmental Prediction's (NCEP) Global Forecast System (GFS) analysis using WRFDA's CV3 background error covariance matrix (Barker et al. 2004). The ensemble was then integrated forward for 12 h using the WRF Model to develop flow-dependent ensemble statistics before the first observations were assimilated at 1800 UTC 27 August. At that time, the ensemble served as the background for two DA cycling experiments: GTS and GTS+IR. The GTS experiment assimilated surface and upper-level observations from the World Meteorological Organization (WMO) Global Telecommunications System (GTS). The GTS+IR experiment assimilated the GTS observations as well as all-sky BTs observed by

channel 5 of the SEVIRI instrument on board the *Meteosat-10* satellite. Channel 5 is sensitive to upper-tropospheric water vapor. Both experiments assimilated observations hourly for 12 h. As mentioned in section 2, this 12-h period represents the time during which the operationally predicted probabilities of genesis are low. More details about each type of observation assimilated will be discussed in the next subsection.

To see the impact of assimilating all-sky IR BTs on the genesis forecasts of Irma, 5-day (120-h) deterministic forecasts were initialized from the analysis mean of each hourly DA cycle. These forecasts used the same WRF physics options described in the previous subsection. To prevent the drift of the regional WRF Model during the DA cycling, analogous to the setup of the operational PSU WRF-EnKF TC forecast system (e.g., Zhang and Weng 2015; Hartman et al. 2021), we replaced the large-scale features (horizontal wavelengths > 1000 km) in the ensemble means of the first (1800 UTC 27 August) and seventh (0000 UTC 28 August) cycles with the large-scale features of the GFS analysis at those times. In other words, we recentered the large-scale component of the ensemble on the large-scale component of the GFS analysis. The large-scale features were isolated using a low-pass filter via the fast Fourier transform. This recentering was done for the zonal (U) and meridional (V) wind fields, as well as perturbation potential temperature (T), water vapor mixing ratio (QVAPOR), perturbation pressure (P), and perturbation geopotential (PH) at all model levels.

c. *Observations assimilated*

This subsection will provide more details about each type of observation assimilated, including choices of quality control, data thinning, and localization procedures.

The GTS observations assimilated in this study include surface observations from synoptic reports and METAR as well as upper-air observations from soundings and atmospheric motion vectors (AMVs) derived from a mixture of geostationary and polar-orbiting satellites. Figure 2b shows the locations of the assimilated surface and sounding observations during the first cycle. These observations, which were not thinned, are confined to the landmasses. During the remaining eleven cycles, the spatial distribution of the surface and sounding observations remained similar to the first cycle. Figure 2c shows the locations of the assimilated AMVs during the first cycle. A quick glance at the spatial structure of the pressure levels of these AMV observations reveals the presence of the AEW from which Irma would later evolve (lower pressure level implies higher cloud top). Note that these observations were not thinned before assimilation. All GTS observations underwent the same quality control procedure. Namely, an observation was discarded during the assimilation process if the absolute value of the observation increment (also known as the "innovation") was greater than 5 times the prescribed observation error, where the prescribed observation error was obtained using version 3.6.1 of the WRFDA package.

All-sky IR BTs assimilated in this study were observed by the SEVIRI instrument on board the *Meteosat-10* satellite. The SEVIRI instrument, with its 12 spectral imaging channels, provides continuous high density (3-km resolution at subsatellite point) observations over much of the Atlantic Ocean, Europe, and Africa with a temporal frequency of one full-disk scan every 15 min (Schmid 2000). In total, 8 of the 12 spectral channels are sensitive to IR wavelengths. Some notable channels include the upper-tropospheric water vapor channel (channel 5; central wavelength of 6.2 μm), the lower-tropospheric water vapor channel (channel 6; central wavelength of 7.3 μm), and the longwave window channel (channel 9; central wavelength of 10.8 μm). To be consistent with F. Zhang et al. (2019), we chose to assimilate the upper-tropospheric water vapor channel in this study. The IR BTs assimilated during the first cycle are shown in Fig. 2d. Once again, the AEW from which Irma evolved is clearly visible. Note that these observations were not assimilated west of 45°W. This decision was made because *Meteosat-10* observations west of that longitude are quite far from the footprint of the satellite. Since that region is very far from the area of concern during the assimilation process, the decision was made to disregard them. In the area east of 45°W, the raw IR BTs have a horizontal resolution of approximately 3 km. These observations were thinned such that we assimilated every eighth observation, or one roughly every 24 km. This results in a horizontal resolution of assimilated IR BTs that was comparable to that of the AMVs.

One of the challenges associated with assimilating all-sky IR BTs is the presence of large representativeness errors that can result from a mismatch between the observed and simulated cloud scenes. To reduce the magnitude of these representativeness errors, and thereby suppress potentially unphysical analysis increments, we adaptively adjusted observation errors via the adaptive observation error inflation (AOEI) method introduced by Minamide and Zhang (2017). AOEI inflates the observation error when the square of the difference between the observed and simulated brightness temperatures exceeds the sum of the uninflated observation error variance and simulated observation error variance. The inflated observation error is thus the observation error variance that maintains the optimal statistical relationship pointed out by Desroziers et al. (2005). This study did not reject any IR observations because it adaptively adjusted the observation error using AOEI.

To deal with underdispersive situations where the forecast ensemble erroneously predicts clear skies despite cloudy observations, we applied the adaptive background error inflation method (ABEI) introduced by Minamide and Zhang (2019). This method inflates the ensemble spread in such problematic regions by applying an empirically derived multiplicative inflation factor over said regions, and then propagating the inflation factor to surrounding areas through the method of Anderson (2009). ABEI is thus a spatially varying multiplicative inflation scheme. Note that ABEI is not designed to create cloud particles during the analysis step, rather it increases the likelihood of producing clouds in the next DA cycle by increasing the ensemble spread over regions where the ensemble is spuriously clear.

Based on the innovation statistics (not shown here), and considering that we were only executing 12 DA cycles, it was determined that bias correction of the IR BTs was not necessary. This is consistent with previous studies (e.g., Zhang et al. 2018; Y. Zhang et al. 2019; Hartman et al. 2021; Chan and Chen 2022)

that have shown that only small IR BT biases are present in the EnKF system. Future work can investigate if bias correction can further enhance the impacts of all-sky IR BT DA.

When assimilating observations in this study, ensemble covariances were localized using the Gaspari and Cohn (1999) fifth-order piecewise polynomial to eliminate the effects of spurious long-distance correlations. The localization radius of influence (ROI) used in the horizontal was 300 km for surface GTS observations [consistent with F. Zhang et al. (2019) and Hartman et al. (2021)], 100 km for upper-air GTS observations [similar to F. Zhang et al. (2019) and Hartman et al. (2021)], and 100 km for all-sky IR BTs. The choice of 100-km ROI in the horizontal for all-sky IR BTs was to make their impact comparable to that of the AMVs. Consistent with F. Zhang et al. (2019) and Hartman et al. (2021), the vertical ROI for all GTS observations was 43 vertical levels. In light of recent studies that have shown complex and nonnegligible vertical correlation structures between upper-tropospheric water vapor channel BTs and state variables extending to the lower troposphere (e.g., Chan and Chen 2022; Zhang et al. 2022), the IR BTs were not vertically localized. It is possible that other localization ROIs may prove to be more optimal than the ones chosen—this can be explored in future work. Furthermore, adaptive localization (e.g., Lei et al. 2020; Wang et al. 2020) of all-sky IR BT observations is a very interesting topic that may be explored in future studies.

4. Results

This section is divided into three parts. In the first part, we describe the tracking algorithm that was used to objectively determine the center of the TC or pre-TC disturbance at each time in the deterministic forecasts. We then compare the performance of the deterministic forecasts in each experiment in the second part. Finally, in the third part, a pouch-centric view of the evolution of dynamic and thermodynamic variables in the forecasts is provided to investigate the potential physical reasons that lead to the forecast improvements.

a. Tracking algorithm

Before comparing the results of individual forecasts, it is necessary to describe the algorithm used to objectively determine the center location of the TC or pre-TC disturbance at each time. This algorithm is loosely based on the study of Majumdar and Torn (2014) in that we used the same quantities. The quantities chosen are motivated by the fact that a tropical cyclone is a warm core cyclonic disturbance with a closed circulation pattern around a local minimum of sea level pressure (SLP). As such, the location of the TC's or pre-TC disturbance's center can be identified using 1) the local maxima in the 700–850-hPa layer-averaged circulation, 2) the local maxima in the 200–850-hPa thickness anomaly (i.e., difference between thickness and domain-averaged thickness), and 3) the local minima in the SLP. Circulation at any grid point was computed by horizontally averaging relative vorticity within a 100 km $\times$ 100 km square centered on said point. Note that prior to identifying the local extrema, the thickness anomaly and SLP fields were smoothed via a 2D boxcar kernel with a length scale of 100 km.

To illustrate the TC tracking algorithm, a snapshot of these three quantities (circulation, smoothed thickness anomaly, and smoothed SLP) and the simulated cloud fields (all four quantities are from the last hour of a forecast) are shown in Fig. 3. Based on the three smoothed quantities in this figure, the apparent location of the TC is indicated by the white "x" in each subplot. Since the postgenesis location of a TC is easier to identify compared to the pregenesis location, we chose to start at the end of each simulation and track the TC or pre-TC disturbance backward in time. This was feasible because every forecast developed a relatively stronger system by the end of its simulation. Specifically, at the end of a forecast we identified the circulation–thickness–SLP trio of local extrema such that 1) all extrema within the trio were within 300 km of one another and 2) the circulation maximum in that trio was the global maximum of circulation. The location of the SLP minimum in the trio was labeled as the TC or pre-TC disturbance center at that last hour of the forecast. To find the TC or pre-TC disturbance center at each subsequent hour working backward in time, we identified the locations of the maximum 700–850-hPa layer-averaged circulation, maximum 200–850-hPa thickness anomaly, and minimum SLP within 100 km of the previously found TC or pre-TC disturbance center. The location of the centroid of the triangle having vertices at these locations was labeled the TC or pre-TC disturbance center at that time. The performance of this tracking algorithm was visually checked and validated with the simulated cloud fields for each hour of every forecast. Results show that the algorithm can successfully track the storm from before its genesis to the end of the 5-day forecast. Animations consisting of all snapshots such as the one in Fig. 3 for every forecast can be viewed in the supplemental material.

b. Comparison of deterministic forecast performance

In this subsection, we compare the performance of the deterministic forecasts for each experiment. The track and intensity forecasts for each experiment are provided in Fig. 4. Note that to quantify intensity, we found the maximum 10-m wind speed within 300 km of the TC or pre-TC disturbance center provided by the tracking algorithm that was described in the previous subsection. Although we do not define a threshold wind speed for genesis in this study, it is safe to say that both the GTS (Fig. 4b$_1$) and GTS+IR (Fig. 4b$_2$) experiments capture the genesis of Irma since all forecasts attain at least tropical storm strength. Furthermore, both experiments predict the RI that occurred in the 48 h after genesis. Additionally, forecasts initialized after 0300 UTC 28 August in both experiments predict the plateau of Irma's intensity in the 48–72 h after genesis.

The most salient difference between the intensity forecasts of the GTS and GTS+IR experiments is the overly premature intensification in the GTS forecasts. This difference grows as we move from the forecasts initialized from the earlier cycles (coolest colors) to the forecasts initialized from the later cycles (warmest colors) and is most prominent for forecasts

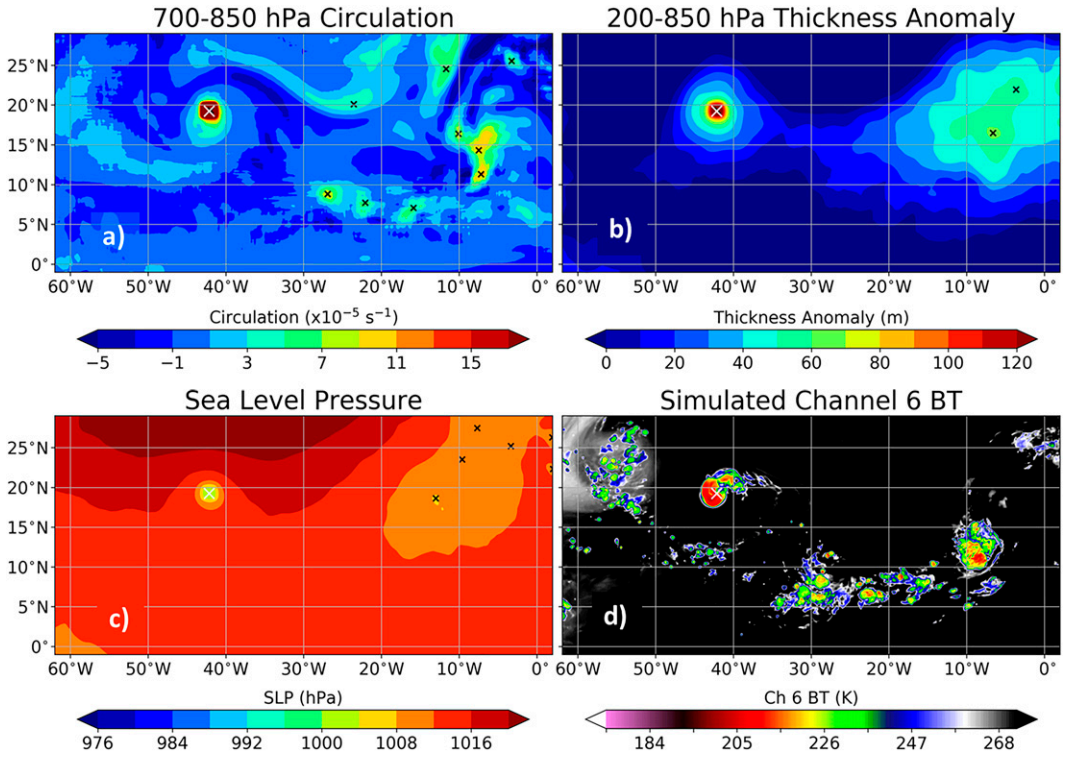

FIG. 3. Snapshot from the last hour of the GTS deterministic forecast initialized at 0500 UTC 28 Aug of the (a) 700–850-hPa layer-averaged circulation, (b) 200–850-hPa thickness anomaly, (c) sea level pressure, and (d) simulated SEVIRI channel-6 BT fields. Each black "x" indicates the location of a local extremum within 150 km while the white "x" shows the location of the TC center at this time as determined by the tracking algorithm described in the text. See section 4a for details on how (a)–(c) were generated. Animations consisting of all such snapshots for every forecast can be viewed in the supplemental material.

initialized after 0100 UTC 28 August. By the last few cycles, the GTS forecasts predict a tropical storm as much as 24 h before Irma entered the NHC's HURDAT2 best track database as a tropical depression (vertical blue dashed line). On the other hand, the assimilation of all-sky IR BTs delays the intensification such that most of the GTS+IR forecasts attain tropical storm status very close to the time of genesis in the best track. Based on this, we conclude that the assimilation of all-sky IR BTs improved the timing of genesis in forecasts of Irma without degrading the forecasts of RI. This conclusion can be drawn without defining a genesis time in the forecasts since a disturbance that has reached tropical storm status and continues to intensify thereafter has clearly undergone genesis at some time prior.

Although the assimilation of all-sky IR BTs improved the timing of genesis, it degraded the track forecasts after genesis relative to the best track (Figs. 4a$_1$,4a$_2$). A southward bias of the GTS+IR forecasts relative to the best track is evident (Fig. 4a$_2$), whereas the GTS forecasts track quite close to the best track (Fig. 4a$_1$). This implies that assimilating all-sky IR BTs might degrade the large-scale steering flow. One potential reason is that the ensemble error correlations between upper-tropospheric clear-sky IR BTs and the dynamical fields are weak (not shown). Hence, the limited ensemble size might lead to an unrealistic update of the large-scale circulation from assimilating upper-tropospheric clear-sky IR BTs. However, the exact reason and potential methodologies to improve the performance of all-sky IR BTs DA deserves future studies, which are out of the scope of the current study.

To determine the potential impact of these track differences on the forecasted genesis timing differences, we initialized another set of 12 forecasts. The initial conditions for these new forecasts were the EnKF analysis means of the GTS+IR experiment with the environmental features replaced with those of the analysis means of the GTS experiment. To do this, a low-pass filter was used to replace the features larger than 1000 km in the zonal (U) and meridional (V) wind fields, as well as perturbation potential temperature (T), water vapor mixing ratio (QVAPOR), perturbation pressure (P), and perturbation geopotential (PH) at all model levels. The results of these new forecasts (GTS + IR*) are shown in Figs. 4a$_3$ and 4b$_3$.

Replacing the large-scale environment of the GTS+IR analyses with the large-scale environment of the GTS analyses substantially reduced the differences between the tracks of the GTS and GTS+IR experiments. Despite this, the timing of genesis in the GTS + IR* forecasts are relatively unchanged relative to the GTS+IR experiment. Furthermore,

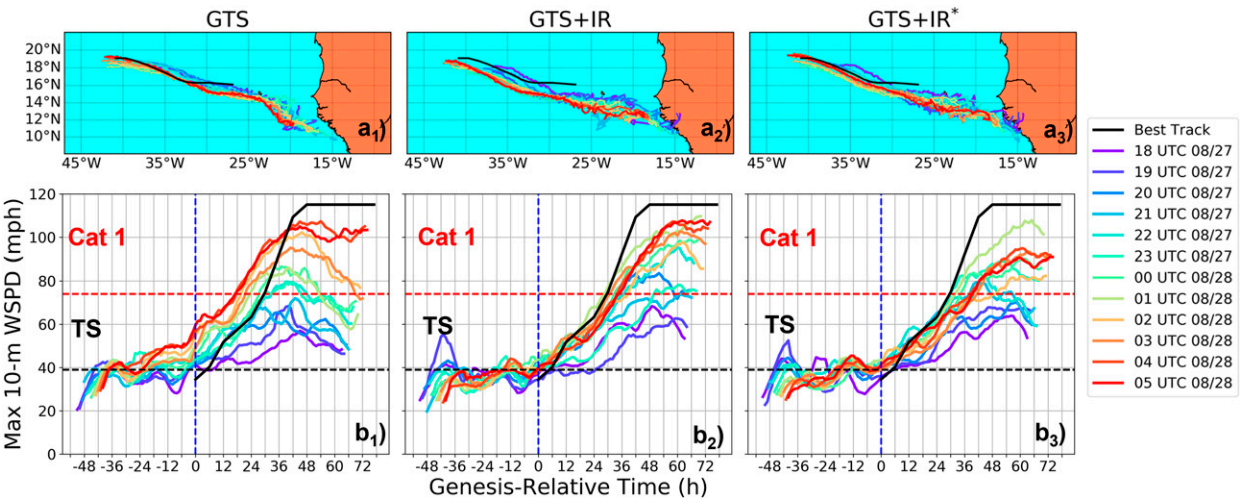

FIG. 4. Deterministic forecasts of (top) track and (bottom) maximum 10-m wind speed within 300 km of the TC center for the (a_1),(b_1) GTS; (a_2),(b_2) GTS+IR; and (a_3),(b_3) GTS + IR* experiments. In each panel, the solid lines plotted in cool colors are the forecasts initialized from the analysis mean of the earlier cycles, while the warm colors are those initialized from the analysis mean of the later cycles. Additionally, the solid black line shows the best track values from the National Hurricane Center HURDAT2 database, and the vertical blue dashed line denotes the time at which Irma entered the best track as a tropical depression. Refer to the text for more details on the GTS + IR* experiment.

analysis (along the tracks) of SSTs, 850–200-hPa environmental shear, and average relative humidity in the layer between 950 and 700 hPa reveal no systematic differences that could explain the intensity differences between the GTS and GTS+IR forecasts (not shown). Based on these findings, it is likely that the improved genesis timing in the GTS+IR forecasts is not simply a result of differences in the large-scale environment or tracks.

c. *Pouch-centric view of deterministic forecasts*

As discussed in the introduction, genesis is a process that involves multiple scales. In this subsection we explore the differences between the GTS and GTS+IR forecasts on subsynoptic scales to elucidate the main reasons why assimilating all-sky IR BTs improved the timing of genesis in forecasts of Irma. To do so, we analyzed the evolution of dynamic and thermodynamic quantities in a frame of reference that is moving with the AEW from which Irma formed. In the analysis that follows, a separate westward phase speed of the AEW at the 850-hPa level was found for each forecast by plotting Hovmöller diagrams of meridional wind speed at those levels. The Hovmöller diagrams were constructed via averaging over the 5°–15°N latitudinal band (similar to Fig. 5 of Wang et al. 2010). On each Hovmöller diagram, we found the longitude–time slope of the zero-contour line separating negative (to the west) and positive (to the east) meridional velocities from forecast initialization time through 20-h pregenesis. This slope was defined as the mean phase speed of the AEW. We did not use the meridional velocities after 20-h pregenesis in the calculation of the phase speed since many forecasts had formed a TC by this point which had likely "shed" from the AEW itself (Dunkerton et al. 2009). The AEW phase speed is then subtracted from the simulated flow fields to provide a pouch-centric view of deterministic forecasts.

As seen by the 850-hPa streamlines in Fig. 5, a closed meso-α-scale circulation (the "pouch") becomes visible after the westward phase speed of the AEW has been subtracted from the flow. The center of this recirculation region, at the intersection of the wave trough and critical latitude (i.e., line of zero AEW-relative zonal wind), is the preferred location for genesis for both dynamic and thermodynamic reasons. Dynamically, it is the focal point for the aggregation of low-level vorticity anomalies and experiences less strain deformation (Montgomery and Enagonio 1998; Schecter and Dubin 1999; Dunkerton et al. 2009). Thermodynamically, moisture lifted above the boundary layer by deep convection accumulates near the pouch center since it is a stagnation point (Wang 2012). A positive feedback loop between the deep convection and meso-α-scale circulation was therefore postulated by Wang (2012) to lead to the formation of an enhanced meso-β-scale vortex near the pouch center that ultimately becomes a tropical depression. More specifically, deep convection strengthens the cyclonic circulation near the pouch center through updrafts' combined influence of vortex stretching and low-level convergence, which accelerates vorticity aggregation. With a stronger circulation to retain moisture, deep convection is amplified. MCVs associated with more organized MCSs may also play a role in the genesis process (Bister and Emanuel 1997; Houze et al. 2009). Considering this feedback loop, genesis timing is therefore determined by the details of the deep convection and its interaction with the meso-α-scale pouch circulation. In the analysis that follows, we will show how differences in the deep convective evolution inside the meso-α-scale pouch led to different genesis timing in the GTS and GTS+IR forecasts.

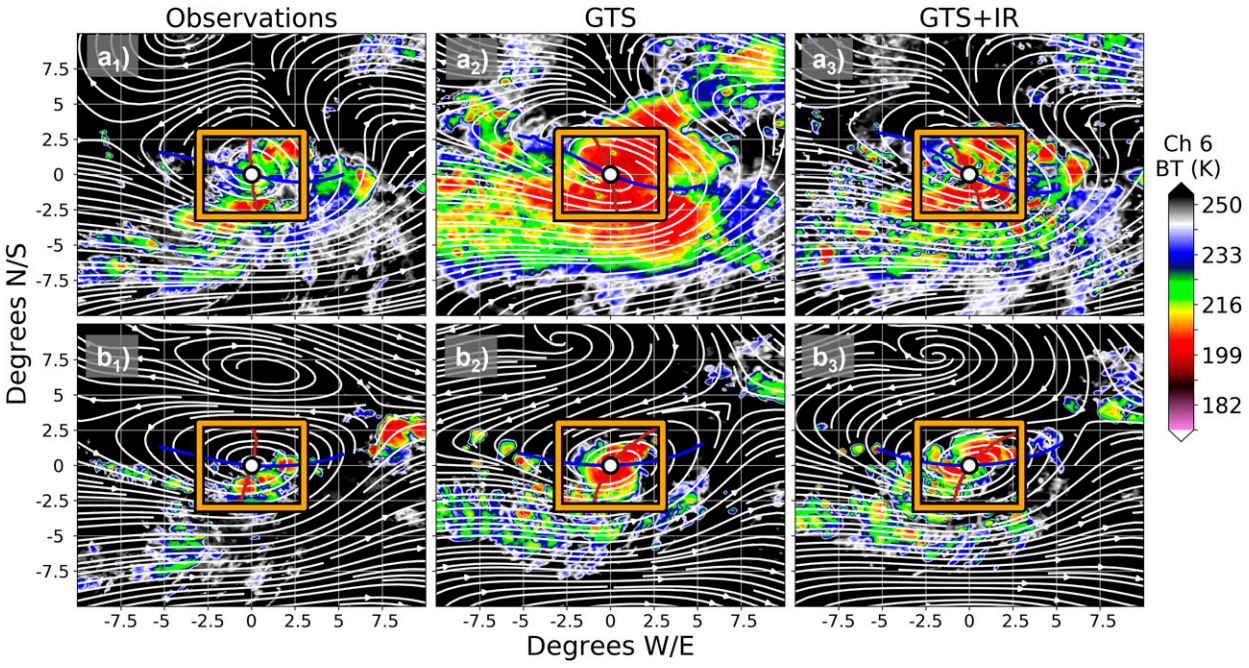

FIG. 5. *Meteosat-10* channel-6 BT overlaid with 850-hPa AEW-relative streamlines, surface trough axis (brown line), wave critical latitude (blue line), and 850-hPa pouch center (white circle) from (a_1) observations and (a_2),(a_3) EnKF analysis mean of each experiment valid at 0400 UTC 28 Aug (44-h pregenesis) as well as (b_1) observations and (b_2),(b_3) forecasts initialized from the analyses in row 1 valid at 0400 UTC 29 Aug (20-h pregenesis). The streamlines, trough axis, critical latitude, and pouch center plotted in (a_1) and (b_1) were identified using the ERA5 reanalysis. The orange box centered on each pouch center is 6° latitude × 6° longitude.

We start this analysis by looking at simulated cloud fields within the 850-hPa pouch. Snapshots of the lower-tropospheric water vapor channel (SEVIRI channel 6) BTs and 850-hPa wave-relative streamlines are shown in Fig. 5 at two times as an example. Note that the ERA5 reanalysis was used to locate the "observed" pouch and pouch center in this example. At 0400 UTC 28 August, the simulated channel-6 BTs of the GTS analysis mean (Fig. 5a_2) reveal a much larger area of low BTs in the pouch compared to the observed channel-6 BTs at the same time (Fig. 5a_1). In fact, the vast majority of the 6° latitude × 6° longitude orange box in the GTS analysis is filled with channel-6 BTs less than 210 K. The GTS+IR analysis at 0400 UTC 28 August (Fig. 5a_3) features a much-reduced area of low simulated channel-6 BTs relative to the GTS analysis as well as finer details in the simulated cloud structures. Although the simulated channel-6 BTs of the GTS+IR analysis are more realistic than the GTS analysis, they still overestimate the areal coverage of low BTs. After 24 h of integration, the simulated channel-6 BTs of the GTS forecast (Fig. 5b_2) are once again less realistic with a greater spatial coverage of low BTs that are more concentrated within the pouch than those of observations (Fig. 5b_1) and the GTS+IR forecast (Fig. 5b_3).

Not only does the GTS simulation produce more clouds than GTS+IR within the 850-hPa pouch at the times selected in Fig. 5, but it also does so at most times leading up to genesis. In Fig. 6, as well as all remaining figures, we choose to focus on the forecasts initialized from the last four cycles (0200–0500 UTC 28 August) since these are the forecasts that feature the most obvious premature genesis in the GTS experiment (Figs. 4b_1 and 6a_1–a_4). Although the average channel-6 BT observation-minus-forecast (OmF) value within a 6° latitude × 6° longitude box centered on the pouch center is always positive leading up to genesis (Figs. 6b_1–b_4) for both experiments, the average BT OmF of the GTS forecasts substantially exceeds that of the GTS+IR forecasts at most times because the all-sky IR observations helped to constrain cloud features. Furthermore, the OmF of the number of grid points having a channel-6 BT less than 205 K within those same boxes is noticeably more negative in the GTS forecasts than the GTS+IR forecasts at most times (Figs. 6c_1–c_4). This indicates that the GTS forecasts have more cold cloud tops than the GTS+IR forecasts. Although both experiments overproduce clouds and overpredict the spatial coverage of cold cloud tops within the pouch relative to the observations at most times, the assimilation of all-sky IR BTs helps to alleviate these biases in the forecasts.

Since the presence of a cold cloud top does not necessarily indicate the presence of deep convection, we choose to analyze composite reflectivity within the 850-hPa pouch. Here, we define convective area as the number of grid points within the 6° latitude × 6° longitude box centered on the pouch center having a composite reflectivity exceeding 35 dB*Z*. A quick inspection of Fig. 7 reveals a larger convective area at most times of the forecasts initialized from the last four EnKF analyses in the GTS experiment than the GTS+IR experiment. In summary, the GTS forecasts that undergo the most obvious premature genesis feature a larger convective area and larger overproduction of cold cloud tops within the pouch than the

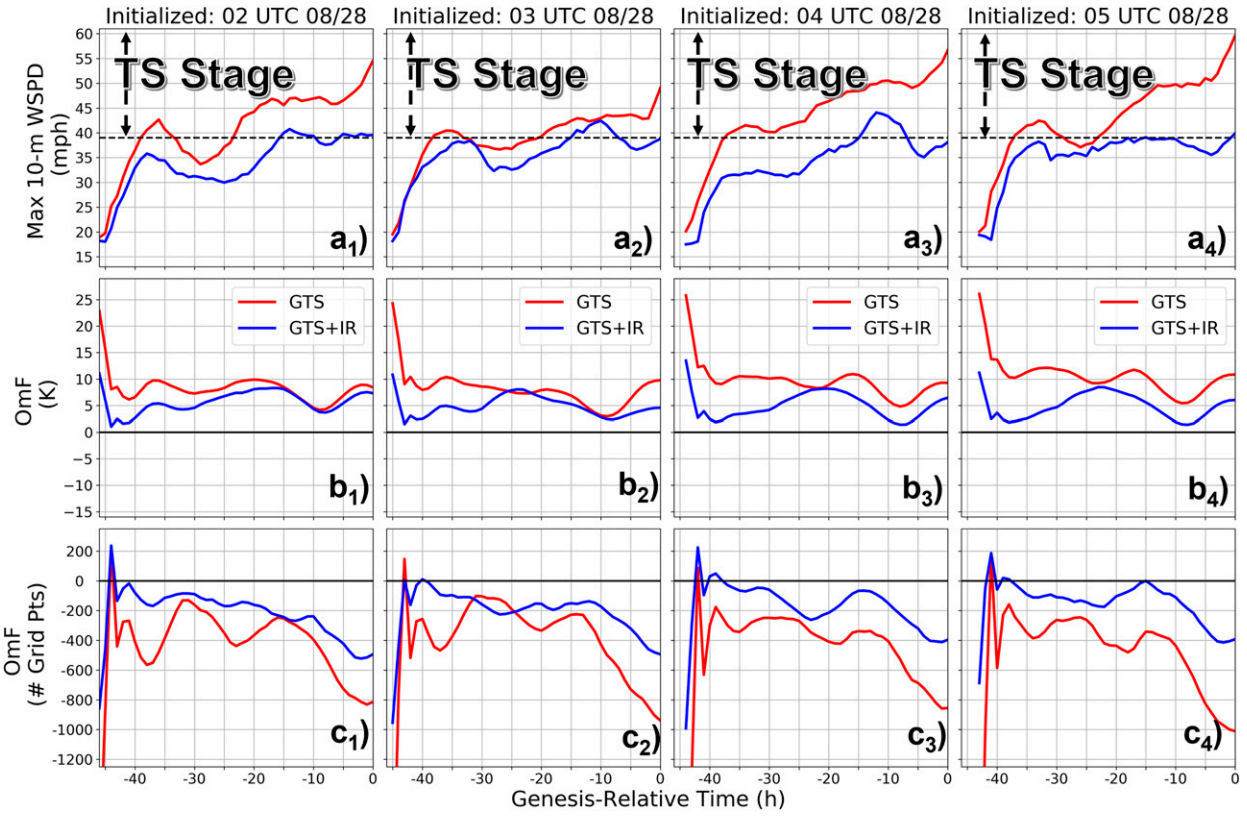

FIG. 6. Comparison of the (a_1)–(a_4) maximum 10-m wind speed within 300 km of the pre-TC center, (b_1)–(b_4) average of *Meteosat-10* channel-6 BT OmF, and (c_1)–(c_4) average of cold cloud top area OmF for forecasts initialized from the 0200 UTC 28 Aug (in column 1) to 0500 UTC 28 Aug (in column 4) EnKF analysis means. Observed 850-hPa pouch center locations were approximated using the ERA5 reanalysis. Grid points in (c_1)–(c_4) were identified as cold cloud tops if the *Meteosat-10* channel-6 BT was less than 205 K. All averages were found over a 6° latitude × 6° longitude box centered on the 850-hPa pouch center.

GTS+IR forecasts. As pointed out by the previous studies, more widespread deep convection within the pouch might be more conductive to TC genesis (e.g., Leppert et al. 2013a,b; Zawislak and Zipser 2014).

To gain a better understanding of why the GTS forecasts produce a larger convective area within the pouch than the GTS+IR forecasts, we look at the evolution of the column saturation fraction (CSF) within the pouch leading up to genesis (Fig. 8). CSF is calculated as the ratio of total precipitable water to saturated precipitable water. A larger CSF is favorable for sustained deep convection because it reduces the effects of entrainment of dry air into convective plumes and limits the development of evaporatively cooled downdrafts (Neelin et al. 2009; Chen et al. 2022b). For the forecasts initialized from the last four EnKF analyses, Fig. 8 shows the GTS ones are generally closer to saturation inside the pouch than the GTS+IR ones. The largest CSF values, which are closest to the pouch center, extend farther outward from the pouch center in the GTS forecasts than in the GTS+IR forecasts. In fact, the GTS pouch features CSF values greater than 90% at radii oftentimes beyond 100 km (Figs. 8a_1–a_4), whereas CSF values greater than 90% in the GTS+IR pouch are mostly confined to within 50 km of the pouch center (Figs. 8b_1–b_4). The larger close-to-saturated area led to more widespread deep convection within the pouch in the GTS experiment. On the other hand, all-sky IR observations provide additional information on cloud and moisture fields. As a result, the initial cloud and moisture fields are better constrained in the GTS+IR experiment.

Now that we have shown a larger portion of the pouch in the GTS forecasts is closer to saturation than the GTS+IR forecasts, we turn our attention to the meso-β-scale region near the pouch center from which the tropical depression likely forms. Figure 9 shows the vertical distribution of relative humidity averaged within a 2° latitude × 2° longitude box centered on the pouch in the hours leading up to genesis. The difference plots (Figs. 9c_1–c_4) reveal a noticeably moister inner pouch at all vertical levels in the GTS forecasts compared to the GTS+IR forecasts, especially in the forecasts initialized from the last three EnKF analyses. This is consistent with the CSF values shown in Fig. 8.

The noticeably moister pouch in the GTS forecasts is not surprising when we consider the vertical profile of the average EnKF analysis increments to water vapor mixing ratio during the DA cycling experiments (Fig. 10). These averages were taken over the whole domain for each cycle and then averaged

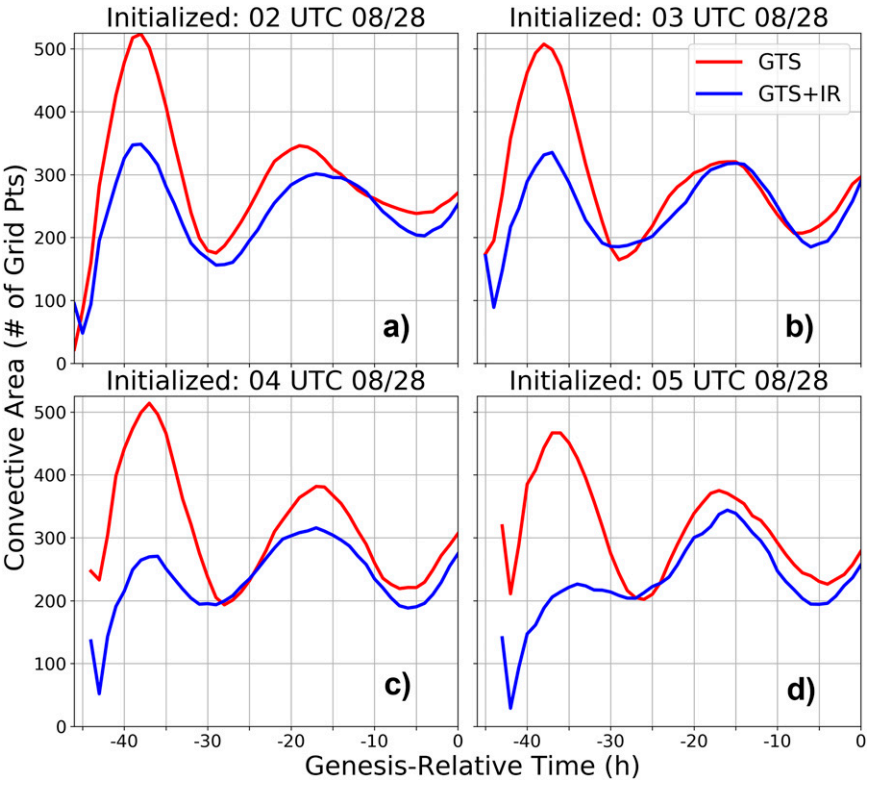

FIG. 7. Convective area within a 6° latitude × 6° longitude box centered on the 850-hPa pouch center for forecasts initialized from the (a) 0200, (b) 0300, (c) 0400, and (d) 0500 UTC 28 Aug EnKF analysis means, where the convective core area is the total number of model grid points exceeding a composite reflectivity value of 35 dB*Z*.

over the 12 cycles. Although Fig. 10 does not show the spatial features of the analysis increments, it reveals that the accumulated impact of the assimilation of the GTS observations in this study is to add moisture to the large-scale environment at all vertical levels. Furthermore, Fig. 10 shows that assimilating all-sky IR BTs removes moisture from the large-scale environment at all vertical levels. Despite the large-scale drying effect of the all-sky IR BT assimilation in this study, the GTS+IR cycling experiment exhibits average water vapor mixing ratio increments that indicate an overall moistening of the large-scale environment between 700 and 925 hPa and an overall drying above 700 hPa and below 925 hPa. The precise details of why the assimilation of GTS observations resulted in moistening of the environment and the assimilation of all-sky IR BTs resulted in drying of the environment is beyond the scope of this study; however, it suffices to say that the pouch in the GTS analyses was moister than the pouch in the GTS+IR analyses (Figs. 8 and 9) and that pouch was likely embedded in a moister environment (Fig. 10). A consequence of the moister GTS pouch and environment is the development and sustenance of widespread deep convection in the forecasts.

Consistent with the moisture differences, there are also differences in dynamic fields within the meso-β-scale region near the pouch center. Figure 11 shows the average relative vorticity in that region surrounding the pouch center for the forecasts initialized from the last four EnKF analyses. Both the GTS (Figs. 11a_1–a_4) and the GTS+IR (Figs. 11b_1–b_4) forecasts feature the spinup of a low-level meso-β-scale vortex well before the time at which the NHC declared genesis. Both forecasts also show the subsequent upward building of the meso-β-scale vortex in the hours after it developed. Despite these similarities, there are some striking differences. Most notably, the spinup of the low-level vortex in the GTS forecast generally occurs approximately 10 h earlier than the GTS+IR forecast. This can be seen by referring to the time between 20- and 30-h pregenesis in Figs. 11c_1, 11c_3, and 11c_4 and between 10- and 20-h pregenesis in Fig. 11c_2. Not only do the GTS forecasts feature the earlier spinup of a low-level vortex, but they also project the subsequent upward building of a stronger, deeper vortex at the meso-β-scale (Figs. 11c_1–c_4) relative to the GTS+IR forecasts.

In both the GTS and GTS+IR forecasts, low-level convergence precedes the spinup of the low-level meso-β vortex (Fig. 12). This is consistent with Wang et al. (2010), who showed that deep convective processes and their associated divergence profile can be the main player in the spinup of a surface vortex. More specifically, low-level convergence induced by convective updrafts helps to spinup the low-level vortex through the aggregation of positive vorticity anomalies as well as vortex stretching near the pouch center. A close

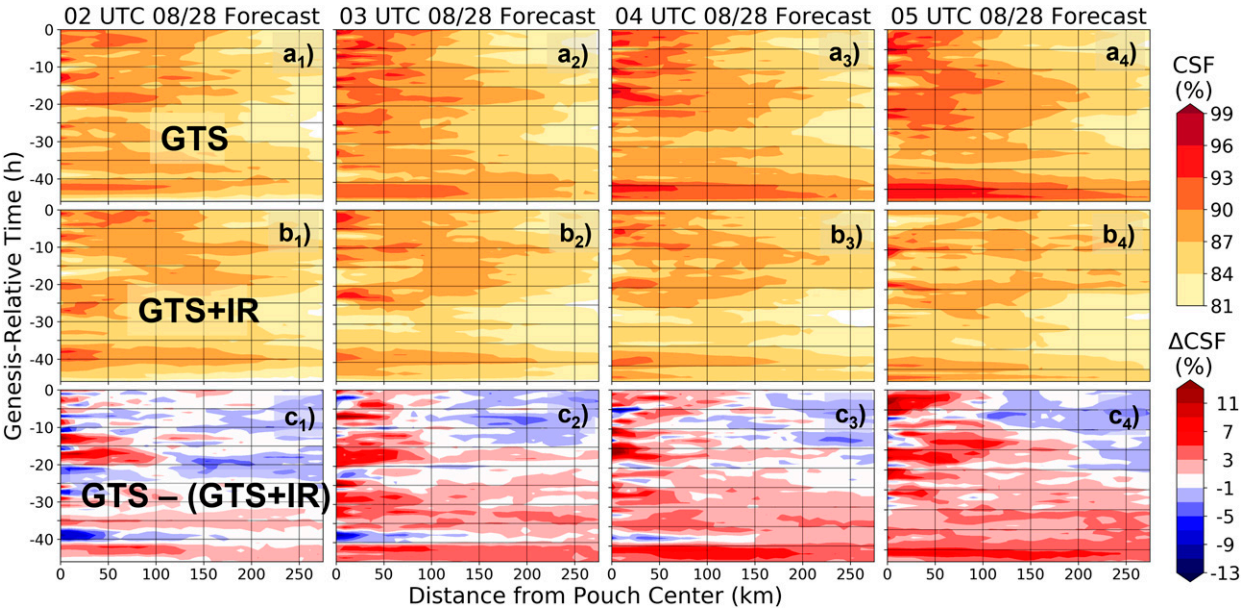

FIG. 8. Column saturation fraction as a function of distance from the 850-hPa pouch center and genesis-relative time for forecasts initialized from the 0200 UTC 28 Aug (in column 1) to 0500 UTC 28 Aug (in column 4) EnKF analysis means of the (a_1)–(a_4) GTS and (b_1)–(b_4) GTS+IR experiments as well as the (c_1)–(c_4) difference between the two.

inspection of Fig. 12 reveals that the low-level convergence in the GTS forecasts is stronger than in the GTS+IR forecasts. The enhanced low-level convergence in the GTS forecasts occurs in conjunction with stronger updrafts (not shown). In short, the GTS forecasts developed a stronger layer of low-level convergence in conjunction with stronger updrafts and an earlier spinup of the low-level meso-β-scale circulation surrounding the more saturated pouch center than the GTS+IR forecasts.

5. Discussion and summary

In the foregoing section, we showed that assimilation of all-sky IR BTs improves the timing of genesis in forecasts of

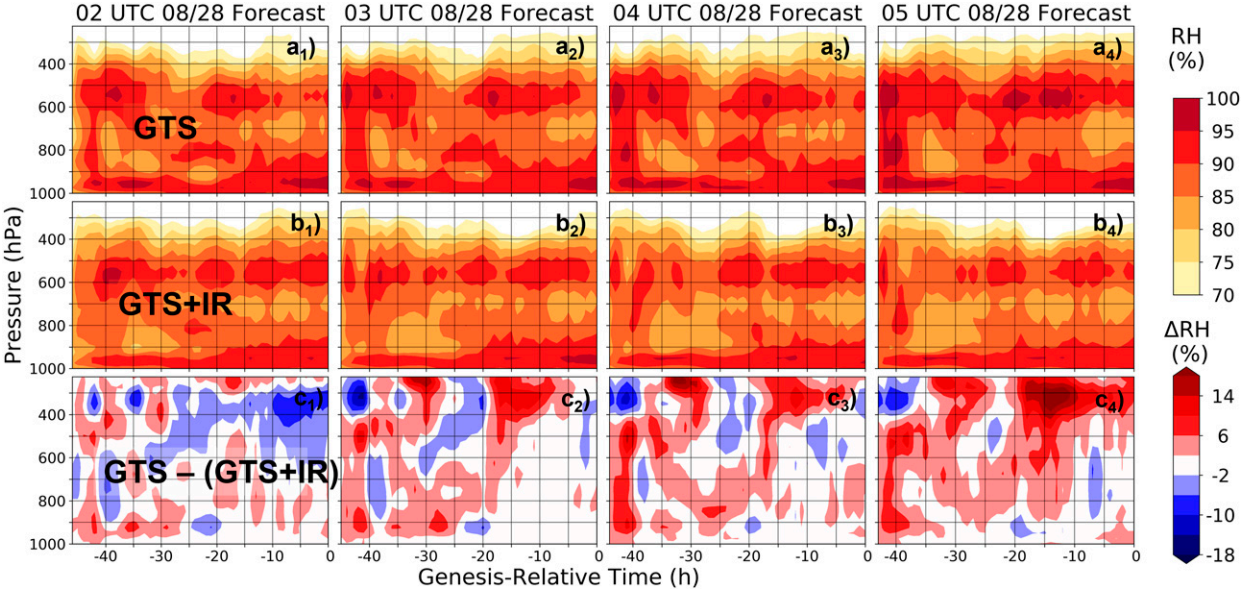

FIG. 9. Temporal evolution of the relative humidity averaged within a 2° latitude × 2° longitude box centered on the 850-hPa pouch center for forecasts initialized from the 0200 UTC 28 Aug (in column 1) to 0500 UTC 28 Aug (in column 4) EnKF analysis means of the (a_1)–(a_4) GTS and (b_1)–(b_4) GTS+IR experiments as well as the (c_1)–(c_4) difference between the two.

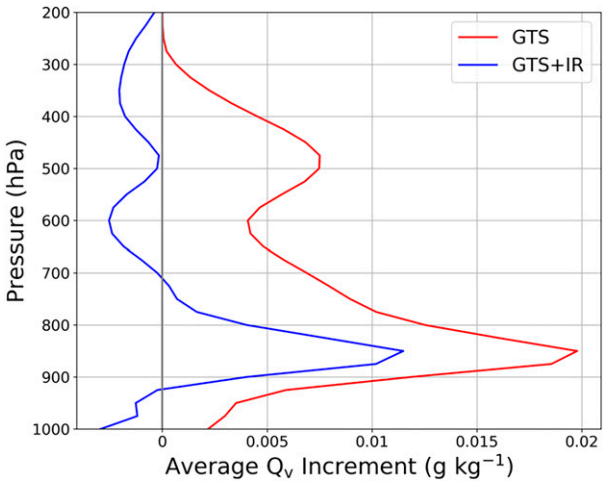

FIG. 10. Vertical variation of the average water vapor mixing ratio increment during the EnKF analyses of each experiment.

Hurricane Irma (2017) by up to 24 h. This improvement is made possible by the removal of presumably excess water vapor at all model levels during the EnKF cycling. Without the assimilation of all-sky IR BTs (GTS), forecasts are initialized with a large-scale environment, as well as meso-α-scale pouch, which is moister and closer to saturation than forecasts that assimilate all-sky IR BTs (GTS+IR). Consequently, the GTS forecasts produce larger areas of deep convection within the pouch, much of which is spurious. The GTS+IR forecasts, on the other hand, produce less spurious deep convection within the pouch owing to less moisture within it and the large-scale environment. With a larger area of deep convection within the pouch, the GTS forecasts produce a stronger layer of low-level convergence relative to the GTS+IR forecasts. This enhanced low-level convergence acts to spinup the low-level meso-β-scale vortex quicker compared to the GTS+IR forecast, ultimately leading to a tropical cyclone sooner.

Recall that the NHC's Tropical Weather Outlook predicted no chance of genesis within 48 h of the times our forecasts were initialized. On the other hand, our baseline experiment (GTS) predicted genesis in all forecasts. This discrepancy is likely because our regional model has a finer grid spacing relative to those of the operational models used to produce the NHC outlook. Additionally, our baseline experiment assimilated high resolution AMVs, whereas the operational models likely assimilated thinned AMVs [e.g., ECMWF (2021)].

The results of this study show that genesis timing is very sensitive to the initial moisture content within the preexisting disturbance. The strong EnKF updates to the moisture content of the environment that ultimately led to improved genesis timing in the case of Irma are made possible by the ensemble correlations that exist between IR BTs and water vapor. Such moisture updates have been shown to dramatically improve forecasts of TC intensification, which is highly sensitive to initial moisture conditions (Emanuel and Zhang 2017). Since deep convection is sensitive to environmental moisture content, it is not surprising that assimilation of all-sky IR BTs improved the timing of genesis in this study through its modulation of the initial moisture conditions. For this specific case, the model simulation without assimilating all-sky IR observations likely overestimated the moisture content within the preexisting disturbance, thereby leading to premature genesis. Unfortunately, we do not have high spatiotemporal in situ observations over the open ocean to constrain the initial moisture content well. Thus, the substantial degradation in the timing of genesis in forecasts will result

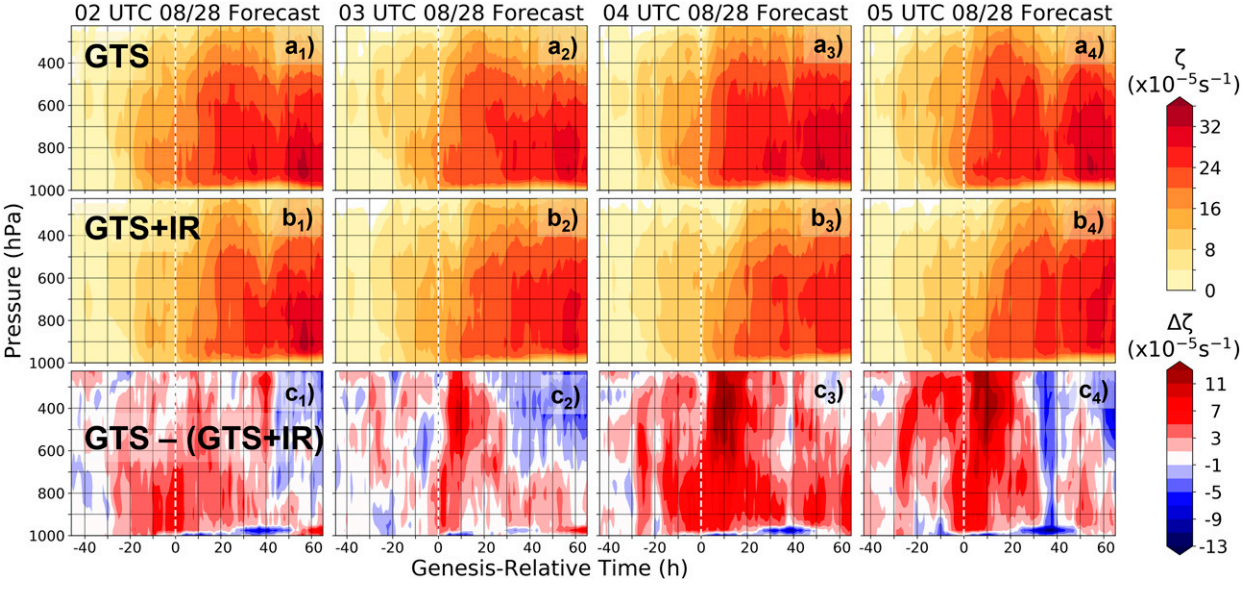

FIG. 11. Temporal evolution of the relative vorticity averaged within a 2° latitude × 2° longitude box centered on the 850-hPa pouch center for forecasts initialized from the 0200 UTC 28 Aug (in column 1) to 0500 UTC 28 Aug (in column 4) EnKF analysis means of the (a_1)–(a_4) GTS and (b_1)–(b_4) GTS+IR experiments as well as the (c_1)–(c_4) difference between the two.

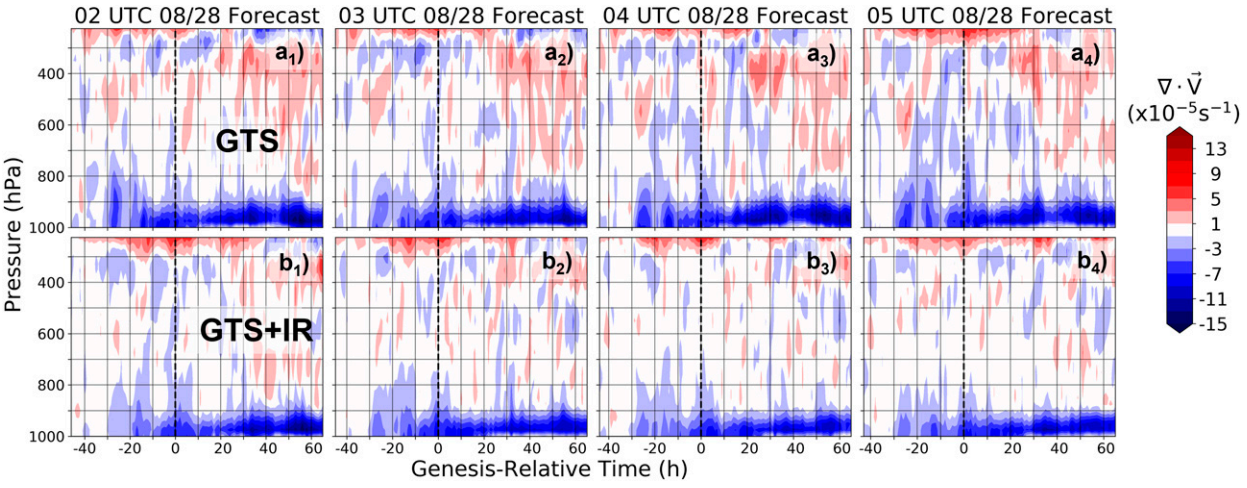

FIG. 12. Temporal evolution of the divergence averaged within a 2° latitude × 2° longitude box centered on the 850-hPa pouch center for forecasts initialized from the 0200 UTC 28 Aug (in column 1) to 0500 UTC 28 Aug (in column 4) EnKF analysis means of the (a_1)–(a_4) GTS and (b_1)–(b_4) GTS+IR experiments.

from either overestimation (e.g., the current case) or underestimation of the initial moisture content. All-sky IR radiances from geo-stationary satellites are arguably the only observation that can provide high resolution observations of clouds and moisture fields over most oceanic basins. Assimilating such information into models could be crucial for the future improvement of TC genesis forecasts.

As a pilot study, we focused on one classic Cape Verde TC case to show the potential of all-sky IR data assimilation to improve TC genesis forecasts and explored the possible physical reasoning that led to the improvement of the forecasts. Future work can and should examine more case studies to determine if the results of this study carry over to other storms. The sensitivity of genesis timing to initial moisture conditions can also be investigated in the future through a series of ensemble sensitivity experiments. Finally, we plan to investigate the sources of the track errors that assimilation of all-sky IR BTs caused in the forecasts of Irma.

Acknowledgments. This work was supported by ONR Grant N00014-18-1-2517, NASA Grant 80NSSC22K0613, NOAA NGGPS and HFIP programs through Subcontract 3004628721 with the University of Michigan, and the Water Cycle and Climate Extremes Modelling (WACCEM) project, which is funded by the U.S. Department of Energy Office of Science Biological and Environmental Research, as part of the Regional and Global Climate Modeling program. Computing was conducted at the Texas Advanced Computing Center (TACC). We thank Eugene Clothiaux and Yunji Zhang for their helpful suggestions throughout the course of this project.

Data availability statement. The EnKF analyses and WRF forecasts presented in this study can be freely downloaded from the Penn State Data Commons (https://doi.org/10.26208/sq9m-wf70). All assimilated GTS observations were obtained from datasets 351.0 and 461.0 of the NCAR Research Data Archive (https://rda.ucar.edu). All assimilated *Meteosat-10* SEVIRI channel-5 BTs were ordered from the EUMETSAT Data Centre (https://www.eumetsat.int/eumetsat-data-centre).

REFERENCES

Anderson, J. L., 2001: An ensemble adjustment Kalman filter for data assimilation. *Mon. Wea. Rev.*, **129**, 2884–2903, https://doi.org/10.1175/1520-0493(2001)129<2884:AEAKFF>2.0.CO;2.

——, 2009: Spatially and temporally varying adaptive covariance inflation for ensemble filters. *Tellus*, **61A**, 72–83, https://doi.org/10.1111/j.1600-0870.2007.00361.x.

——, and N. Collins, 2007: Scalable implementations of ensemble filter algorithms for data assimilation. *J. Atmos. Oceanic Technol.*, **24**, 1452–1463, https://doi.org/10.1175/JTECH2049.1.

Asaadi, A., G. Brunet, and M. K. Yau, 2016: On the dynamics of the formation of the Kelvin cat's-eye in tropical cyclogenesis. Part II: Numerical simulation. *J. Atmos. Sci.*, **73**, 2339–2359, https://doi.org/10.1175/JAS-D-15-0237.1.

——, ——, and ——, 2017: The importance of critical layer in differentiating developing from nondeveloping easterly waves. *J. Atmos. Sci.*, **74**, 409–417, https://doi.org/10.1175/JAS-D-16-0085.1.

Barker, D. M., W. Huang, Y.-R. Guo, A. J. Bourgeois, and Q. N. Xiao, 2004: A three-dimensional variational data assimilation system for MM5: Implementation and initial results. *Mon. Wea. Rev.*, **132**, 897–914, https://doi.org/10.1175/1520-0493(2004)132<0897:ATVDAS>2.0.CO;2.

Bell, M. M., and M. T. Montgomery, 2019: Mesoscale processes during the genesis of Hurricane Karl (2010). *J. Atmos. Sci.*, **76**, 2235–2255, https://doi.org/10.1175/JAS-D-18-0161.1.

Bister, M., and K. A. Emanuel, 1997: The genesis of Hurricane Guillermo: TEXMEX analyses and a modeling study. *Mon. Wea. Rev.*, **125**, 2662–2682, https://doi.org/10.1175/1520-0493(1997)125<2662:TGOHGT>2.0.CO;2.

Braun, S. A., M. T. Montgomery, K. J. Mallen, and P. D. Reasor, 2010: Simulation and interpretation of the genesis of Tropical Storm Gert (2005) as part of the NASA tropical cloud

systems and processes experiment. *J. Atmos. Sci.*, **67**, 999–1025, https://doi.org/10.1175/2009JAS3140.1.

——, and Coauthors, 2013: NASA's Genesis and Rapid Intensification Processes (GRIP) field experiment. *Bull. Amer. Meteor. Soc.*, **94**, 345–363, https://doi.org/10.1175/BAMS-D-11-00232.1.

Briegel, L. M., and W. M. Frank, 1997: Large-scale influences on tropical cyclogenesis in the western North Pacific. *Mon. Wea. Rev.*, **125**, 1397–1413, https://doi.org/10.1175/1520-0493(1997)125<1397:LSIOTC>2.0.CO;2.

Cangialosi, J. P., A. S. Latto, and R. Berg, 2018: National Hurricane Center Tropical Cyclone Report: Hurricane Irma (AL112017) 30 August–12 September 2017. NHC Tech. Rep., 111 pp., https://www.nhc.noaa.gov/data/tcr/AL112017_Irma.pdf.

Chan, M.-Y., and X. Chen, 2022: Improving the analyses and forecasts of a tropical squall line using upper tropospheric infrared satellite observations. *Adv. Atmos. Sci.*, **39**, 733–746, https://doi.org/10.1007/s00376-021-0449-8.

——, F. Zhang, X. Chen, and L. R. Leung, 2020: Potential impacts of assimilating all-sky satellite infrared radiances on convection-permitting analysis and prediction of tropical convection. *Mon. Wea. Rev.*, **148**, 3203–3224, https://doi.org/10.1175/MWR-D-19-0343.1.

Chang, M., C.-H. Ho, M.-S. Park, J. Kim, and M.-H. Ahn, 2017: Multiday evolution of convective bursts during western North Pacific tropical cyclone development and nondevelopment using geostationary satellite measurements. *J. Geophys. Res. Atmos.*, **122**, 1635–1649, https://doi.org/10.1002/2016JD025535.

Chen, X., and F. Zhang, 2019: Relative roles of preconditioning moistening and global circumnavigating mode on the MJO convective initiation during DYNAMO. *Geophys. Res. Lett.*, **46**, 1079–1087, https://doi.org/10.1029/2018GL080987.

——, O. M. Pauluis, L. R. Leung, and F. Zhang, 2018a: Multiscale atmospheric overturning of the Indian summer monsoon as seen through isentropic analysis. *J. Atmos. Sci.*, **75**, 3011–3030, https://doi.org/10.1175/JAS-D-18-0068.1.

——, ——, and F. Zhang, 2018b: Atmospheric overturning across multiple scales of an MJO event during the CINDY/DYNAMO campaign. *J. Atmos. Sci.*, **75**, 381–399, https://doi.org/10.1175/JAS-D-17-0060.1.

——, L. R. Leung, Z. Feng, F. Song, and Q. Yang, 2021a: Mesoscale convective systems dominate the energetics of the South Asian summer monsoon onset. *Geophys. Res. Lett.*, **48**, e2021GL094873, https://doi.org/10.1029/2021GL094873.

——, R. G. Nystrom, C. A. Davis, and C. M. Zarzycki, 2021b: Dynamical structures of cross-domain forecast error covariance of a simulated tropical cyclone in a convection-permitting coupled atmosphere–ocean model. *Mon. Wea. Rev.*, **149**, 41–63, https://doi.org/10.1175/MWR-D-20-0116.1.

——, L. R. Leung, Z. Feng, and F. Song, 2022a: Crucial role of mesoscale convective systems in the vertical mass, water, and energy transports of the South Asian summer monsoon. *J. Climate*, **35**, 91–108, https://doi.org/10.1175/JCLI-D-21-0124.1.

——, ——, ——, and Q. Yang, 2022b: Precipitation-moisture coupling over tropical oceans: Sequential roles of shallow, deep, and mesoscale convective systems. *Geophys. Res. Lett.*, **49**, e2022GL097836, https://doi.org/10.1029/2022GL097836.

DeMaria, M., J. A. Knaff, and B. H. Connell, 2001: A tropical cyclone genesis parameter for the tropical Atlantic. *Wea. Forecasting*, **16**, 219–233, https://doi.org/10.1175/1520-0434(2001)016<0219:ATCGPF>2.0.CO;2.

Desroziers, G., L. Berre, B. Chapnik, and P. Poli, 2005: Diagnosis of observation, background and analysis-error statistics in observation space. *Quart. J. Roy. Meteor. Soc.*, **131**, 3385–3396, https://doi.org/10.1256/qj.05.108.

Dunkerton, T. J., M. T. Montgomery, and Z. Wang, 2009: Tropical cyclogenesis in a tropical wave critical layer: Easterly waves. *Atmos. Chem. Phys.*, **9**, 5587–5646, https://doi.org/10.5194/acp-9-5587-2009.

ECMWF, 2021: IFS documentation CY47R3—Part I: Observations. ECMWF, 82 pp., https://doi.org/10.21957/ycow5yjr1.

Emanuel, K., 2018: 100 years of progress in tropical cyclone research. *A Century of Progress in Atmospheric and Related Sciences: Celebrating the American Meteorological Society Centennial*, *Meteor. Monogr.*, No. 59, Amer. Meteor. Soc., https://doi.org/10.1175/AMSMONOGRAPHS-D-18-0016.1.

——, and F. Zhang, 2017: The role of inner-core moisture in tropical cyclone predictability and practical forecast skill. *J. Atmos. Sci.*, **74**, 2315–2324, https://doi.org/10.1175/JAS-D-17-0008.1.

Gaspari, G., and S. E. Cohn, 1999: Construction of correlation functions in two and three dimensions. *Quart. J. Roy. Meteor. Soc.*, **125**, 723–757, https://doi.org/10.1002/qj.49712555417.

Gray, W. M., 1968: Global view of the origin of tropical disturbances and storms. *Mon. Wea. Rev.*, **96**, 669–700, https://doi.org/10.1175/1520-0493(1968)096<0669:GVOTOO>2.0.CO;2.

Green, B. W., and F. Zhang, 2013: Impacts of air–sea flux parameterizations on the intensity and structure of tropical cyclones. *Mon. Wea. Rev.*, **141**, 2308–2324, https://doi.org/10.1175/MWR-D-12-00274.1.

Han, Y., P. van Delst, Q. Liu, F. Weng, B. Yan, R. Treadon, and J. Derber, 2006: JCSDA Community Radiative Transfer Model (CRTM): Version 1. NOAA Tech. Rep. NESDIS 122, 33 pp., https://repository.library.noaa.gov/view/noaa/1157.

——, F. Weng, Q. Liu, and P. van Delst, 2007: A fast radiative transfer model for SSMIS upper atmosphere sounding channels. *J. Geophys. Res.*, **112**, D11121, https://doi.org/10.1029/2006JD008208.

Hartman, C. M., X. Chen, E. E. Clothiaux, and M.-Y. Chan, 2021: Improving the analysis and forecast of Hurricane Dorian (2019) with simultaneous assimilation of *GOES-16* all-sky infrared brightness temperatures and tail Doppler radar radial velocities. *Mon. Wea. Rev.*, **149**, 2193–2212, https://doi.org/10.1175/MWR-D-20-0338.1.

He, J., and Coauthors, 2019: Development and evaluation of an ensemble-based data assimilation system for regional reanalysis over the Tibetan Plateau and surrounding regions. *J. Adv. Model. Earth Syst.*, **11**, 2503–2522, https://doi.org/10.1029/2019MS001665.

Hendricks, E. A., M. T. Montgomery, and C. A. Davis, 2004: The role of "vortical" hot towers in the formation of Tropical Cyclone Diana (1984). *J. Atmos. Sci.*, **61**, 1209–1232, https://doi.org/10.1175/1520-0469(2004)061<1209:TROVHT>2.0.CO;2.

Honda, T., and Coauthors, 2018: Assimilating all-sky *Himawari-8* satellite infrared radiances: A case of Typhoon Soudelor (2015). *Mon. Wea. Rev.*, **146**, 213–229, https://doi.org/10.1175/MWR-D-16-0357.1.

Hong, S.-Y., Y. Noh, and J. Dudhia, 2006: A new vertical diffusion package with an explicit treatment of entrainment processes. *Mon. Wea. Rev.*, **134**, 2318–2341, https://doi.org/10.1175/MWR3199.1.

Houze, R. A., W.-C. Lee, and M. M. Bell, 2009: Convective contribution to the genesis of Hurricane Ophelia (2005). *Mon. Wea. Rev.*, **137**, 2778–2800, https://doi.org/10.1175/2009MWR2727.1.

Iacono, M. J., J. S. Delamere, E. J. Mlawer, M. W. Shephard, S. A. Clough, and W. D. Collins, 2008: Radiative forcing by long-lived greenhouse gases: Calculations with the AER

radiative transfer models. *J. Geophys. Res.*, **113**, D13103, https://doi.org/10.1029/2008JD009944.

Jones, T. A., and Coauthors, 2020: Assimilation of *GOES-16* radiances and retrievals into the Warn-on-Forecast System. *Mon. Wea. Rev.*, **148**, 1829–1859, https://doi.org/10.1175/MWR-D-19-0379.1.

Kerns, B. W., and S. S. Chen, 2013: Cloud clusters and tropical cyclogenesis: Developing and nondeveloping systems and their large-scale environment. *Mon. Wea. Rev.*, **141**, 192–210, https://doi.org/10.1175/MWR-D-11-00239.1.

Lei, L., J. S. Whitaker, J. L. Anderson, and Z. Tan, 2020: Adaptive localization for satellite radiance observations in an ensemble Kalman filter. *J. Adv. Model. Earth Syst.*, **12**, e2019MS001693, https://doi.org/10.1029/2019MS001693.

Leppert, K. D., D. J. Cecil, and W. A. Petersen, 2013a: Relation between tropical easterly waves, convection, and tropical cyclogenesis: A Lagrangian perspective. *Mon. Wea. Rev.*, **141**, 2649–2668, https://doi.org/10.1175/MWR-D-12-00217.1.

——, W. A. Petersen, and D. J. Cecil, 2013b: Electrically active convection in tropical easterly waves and implications for tropical cyclogenesis in the Atlantic and east Pacific. *Mon. Wea. Rev.*, **141**, 542–556, https://doi.org/10.1175/MWR-D-12-00174.1.

Li, Z., and Z. Pu, 2014: Numerical simulations of the genesis of Typhoon Nuri (2008): Sensitivity to initial conditions and implications for the roles of intense convection and moisture conditions. *Wea. Forecasting*, **29**, 1402–1424, https://doi.org/10.1175/WAF-D-14-00003.1.

Majumdar, S. J., and R. D. Torn, 2014: Probabilistic verification of global and mesoscale ensemble forecasts of tropical cyclogenesis. *Wea. Forecasting*, **29**, 1181–1198, https://doi.org/10.1175/WAF-D-14-00028.1.

Meng, Z., and F. Zhang, 2008: Tests of an ensemble Kalman filter for mesoscale and regional-scale data assimilation. Part III: Comparison with 3DVAR in a real-data case study. *Mon. Wea. Rev.*, **136**, 522–540, https://doi.org/10.1175/2007MWR2106.1.

Minamide, M., and F. Zhang, 2017: Adaptive observation error inflation for assimilating all-sky satellite radiance. *Mon. Wea. Rev.*, **145**, 1063–1081, https://doi.org/10.1175/MWR-D-16-0257.1.

——, and ——, 2018: Assimilation of all-sky infrared radiances from *Himawari-8* and impacts of moisture and hydrometer initialization on convection-permitting tropical cyclone prediction. *Mon. Wea. Rev.*, **146**, 3241–3258, https://doi.org/10.1175/MWR-D-17-0367.1.

——, and ——, 2019: An adaptive background error inflation method for assimilating all-sky radiances. *Quart. J. Roy. Meteor. Soc.*, **145**, 805–823, https://doi.org/10.1002/qj.3466.

——, ——, and E. E. Clothiaux, 2020: Nonlinear forecast error growth of rapidly intensifying Hurricane Harvey (2017) examined through convection-permitting ensemble assimilation of *GOES-16* all-sky radiances. *J. Atmos. Sci.*, **77**, 4277–4296, https://doi.org/10.1175/JAS-D-19-0279.1.

Montgomery, M. T., and J. Enagonio, 1998: Tropical cyclogenesis via convectively forced vortex Rossby waves in a three-dimensional quasigeostrophic model. *J. Atmos. Sci.*, **55**, 3176–3207, https://doi.org/10.1175/1520-0469(1998)055<3176:TCVCFV>2.0.CO;2.

——, M. E. Nicholls, T. A. Cram, and A. B. Saunders, 2006: A vortical hot tower route to tropical cyclogenesis. *J. Atmos. Sci.*, **63**, 355–386, https://doi.org/10.1175/JAS3604.1.

——, L. L. Lussier III, R. W. Moore, and Z. Wang, 2010a: The genesis of Typhoon Nuri as observed during the Tropical Cyclone Structure 2008 (TCS-08) field experiment–Part 1: The role of the easterly wave critical layer. *Atmos. Chem. Phys.*, **10**, 9879–9900, https://doi.org/10.5194/acp-10-9879-2010.

——, Z. Wang, and T. J. Dunkerton, 2010b: Coarse, intermediate and high resolution numerical simulations of the transition of a tropical wave critical layer to a tropical storm. *Atmos. Chem. Phys.*, **10**, 10 803–10 827, https://doi.org/10.5194/acp-10-10803-2010.

——, and Coauthors, 2012: The Pre-Depression Investigation of Cloud-Systems in the Tropics (PREDICT) experiment: Scientific basis, new analysis tools, and some first results. *Bull. Amer. Meteor. Soc.*, **93**, 153–172, https://doi.org/10.1175/BAMS-D-11-00046.1.

Neelin, J. D., O. Peters, and K. Hales, 2009: The transition to strong convection. *J. Atmos. Sci.*, **66**, 2367–2384, https://doi.org/10.1175/2009JAS2962.1.

Nolan, D. S., 2007: What is the trigger for tropical cyclogenesis? *Aust. Meteor. Mag.*, **56**, 241–266.

Nunez Ocasio, K. M., 2021: Tropical cyclogenesis and its relation to interactions between African easterly waves and mesoscale convective systems. Ph.D. dissertation, The Pennsylvania State University, 123 pp., https://etda.libraries.psu.edu/catalog/21775kmn18.

Ou, T., D. Chen, X. Chen, C. Lin, K. Yang, H.-W. Lai, and F. Zhang, 2020: Simulation of summer precipitation diurnal cycles over the Tibetan Plateau at the gray-zone grid spacing for cumulus parameterization. *Climate Dyn.*, **54**, 3525–3539, https://doi.org/10.1007/s00382-020-05181-x.

Rajasree, V. P. M., A. P. Kesarkar, J. N. Bhate, V. Singh, U. Umakanth, and T. H. Varma, 2016a: A comparative study on the genesis of North Indian Ocean Tropical Cyclone Madi (2013) and Atlantic Ocean Tropical Cyclone Florence (2006). *J. Geophys. Res. Atmos.*, **121**, 13 826–13 858, https://doi.org/10.1002/2016JD025412.

——, ——, ——, U. Umakanth, V. Singh, and T. Harish Varma, 2016b: Appraisal of recent theories to understand cyclogenesis pathways of Tropical Cyclone Madi (2013). *J. Geophys. Res. Atmos.*, **121**, 8949–8982, https://doi.org/10.1002/2016JD025188.

Reasor, P. D., M. T. Montgomery, and L. F. Bosart, 2005: Mesoscale observations of the genesis of Hurricane Dolly (1996). *J. Atmos. Sci.*, **62**, 3151–3171, https://doi.org/10.1175/JAS3540.1.

Reed, R. J., D. C. Norquist, and E. E. Recker, 1977: The structure and properties of African wave disturbances as observed during phase III of GATE. *Mon. Wea. Rev.*, **105**, 317–333, https://doi.org/10.1175/1520-0493(1977)105<0317:TSAPOA>2.0.CO;2.

Ritchie, E. A., and G. J. Holland, 1997: Scale interactions during the formation of Typhoon Irving. *Mon. Wea. Rev.*, **125**, 1377–1396, https://doi.org/10.1175/1520-0493(1997)125<1377:SIDTFO>2.0.CO;2.

Russell, J. O., A. Aiyyer, J. D. White, and W. Hannah, 2017: Revisiting the connection between African easterly waves and Atlantic tropical cyclogenesis. *Geophys. Res. Lett.*, **44**, 587–595, https://doi.org/10.1002/2016GL071236.

Sawada, Y., K. Okamoto, M. Kunii, and T. Miyoshi, 2019: Assimilating every-10-minute Himawari-8 infrared radiances to improve convective predictability. *J. Geophys. Res. Atmos.*, **124**, 2546–2561, https://doi.org/10.1029/2018JD029643.

Schecter, D. A., and D. H. E. Dubin, 1999: Vortex motion driven by a background vorticity gradient. *Phys. Rev. Lett.*, **83**, 2191–2194, https://doi.org/10.1103/PhysRevLett.83.2191.

Schmid, J., 2000: The SEVIRI instrument. *Proc. 2000 EUMETSAT Meteorological Satellite Data User's Conf.*, Bologna, Italy, EUMETSAT, 10 pp., https://www-cdn.eumetsat.int/files/2020-04/pdf_ten_msg_seviri_instrument.pdf.

Shin, S., and R. K. Smith, 2008: Tropical-cyclone intensification and predictability in a minimal three-dimensional model. *Quart. J. Roy. Meteor. Soc.*, **134**, 1661–1671, https://doi.org/10.1002/qj.327.

Simpson, J., E. Ritchie, G. J. Holland, J. Halverson, and S. Stewart, 1997: Mesoscale interactions in tropical cyclone genesis. *Mon. Wea. Rev.*, **125**, 2643–2661, https://doi.org/10.1175/1520-0493(1997)125<2643:MIITCG>2.0.CO;2.

Sippel, J. A., J. W. Nielsen-Gammon, and S. E. Allen, 2006: The multiple-vortex nature of tropical cyclogenesis. *Mon. Wea. Rev.*, **134**, 1796–1814, https://doi.org/10.1175/MWR3165.1.

Skamarock, W. C., and Coauthors, 2008: A description of the Advanced Research WRF version 3. NCAR Tech. Note NCAR/TN-475+STR, 113 pp., https://doi.org/10.5065/D68S4MVH.

Tang, B. H., and Coauthors, 2020: Recent advances in research on tropical cyclogenesis. *Trop. Cyclone Res. Rev.*, **9**, 87–105, https://doi.org/10.1016/j.tcrr.2020.04.004.

Tarantola, A., 1987: *Inverse Problem Theory*. Elsevier, 644 pp.

Thompson, G., P. R. Field, R. M. Rasmussen, and W. D. Hall, 2008: Explicit forecasts of winter precipitation using an improved bulk microphysics scheme. Part II: Implementation of a new snow parameterization. *Mon. Wea. Rev.*, **136**, 5095–5115, https://doi.org/10.1175/2008MWR2387.1.

Tory, K. J., M. T. Montgomery, and N. E. Davidson, 2006a: Prediction and diagnosis of tropical cyclone formation in an NWP system. Part I: The critical role of vortex enhancement in deep convection. *J. Atmos. Sci.*, **63**, 3077–3090, https://doi.org/10.1175/JAS3764.1.

——, ——, ——, and J. D. Kepert, 2006b: Prediction and diagnosis of tropical cyclone formation in an NWP system. Part II: A diagnosis of Tropical Cyclone Chris formation. *J. Atmos. Sci.*, **63**, 3091–3113, https://doi.org/10.1175/JAS3765.1.

Van Sang, N., R. K. Smith, and M. T. Montgomery, 2008: Tropical-cyclone intensification and predictability in three dimensions. *Quart. J. Roy. Meteor. Soc.*, **134**, 563–582, https://doi.org/10.1002/qj.235.

Wang, C., L. Lei, Z.-M. Tan, and K. Chu, 2020: Adaptive localization for tropical cyclones with satellite radiances in an ensemble Kalman filter. *Front. Earth Sci.*, **8**, 39, https://doi.org/10.3389/feart.2020.00039.

Wang, S., A. H. Sobel, F. Zhang, Y. Q. Sun, Y. Yue, and L. Zhou, 2015: Regional simulation of the October and November MJO events observed during the CINDY/DYNAMO field campaign at gray zone resolution. *J. Climate*, **28**, 2097–2119, https://doi.org/10.1175/JCLI-D-14-00294.1.

Wang, Z., 2012: Thermodynamic aspects of tropical cyclone formation. *J. Atmos. Sci.*, **69**, 2433–2451, https://doi.org/10.1175/JAS-D-11-0298.1.

——, 2018: What is the key feature of convection leading up to tropical cyclone formation? *J. Atmos. Sci.*, **75**, 1609–1629, https://doi.org/10.1175/JAS-D-17-0131.1.

——, M. T. Montgomery, and T. J. Dunkerton, 2010: Genesis of Pre–Hurricane Felix (2007). Part I: The role of the easterly wave critical layer. *J. Atmos. Sci.*, **67**, 1711–1729, https://doi.org/10.1175/2009JAS3420.1.

Weng, F., 2007: Advances in radiative transfer modeling in support of satellite data assimilation. *J. Atmos. Sci.*, **64**, 3799–3807, https://doi.org/10.1175/2007JAS2112.1.

Whitaker, J. S., and T. M. Hamill, 2002: Ensemble data assimilation without perturbed observations. *Mon. Wea. Rev.*, **130**, 1913–1924, https://doi.org/10.1175/1520-0493(2002)130<1913:EDAWPO>2.0.CO;2.

Ying, Y., and F. Zhang, 2017: Practical and intrinsic predictability of multiscale weather and convectively coupled equatorial waves during the active phase of an MJO. *J. Atmos. Sci.*, **74**, 3771–3785, https://doi.org/10.1175/JAS-D-17-0157.1.

——, and ——, 2018: Potentials in improving predictability of multiscale tropical weather systems evaluated through ensemble assimilation of simulated satellite-based observations. *J. Atmos. Sci.*, **75**, 1675–1698, https://doi.org/10.1175/JAS-D-17-0245.1.

Zawislak, J., and E. J. Zipser, 2014: A multisatellite investigation of the convective properties of developing and nondeveloping tropical disturbances. *Mon. Wea. Rev.*, **142**, 4624–4645, https://doi.org/10.1175/MWR-D-14-00028.1.

Zhang, F., and Y. Weng, 2015: Predicting hurricane intensity and associated hazards: A five-year real-time forecast experiment with assimilation of airborne Doppler radar observations. *Bull. Amer. Meteor. Soc.*, **96**, 25–33, https://doi.org/10.1175/BAMS-D-13-00231.1.

——, C. Snyder, and J. Sun, 2004: Impacts of initial estimate and observation availability on convective-scale data assimilation with an ensemble Kalman filter. *Mon. Wea. Rev.*, **132**, 1238–1253, https://doi.org/10.1175/1520-0493(2004)132<1238:IOIEAO>2.0.CO;2.

——, S. Taraphdar, and S. Wang, 2017: The role of global circumnavigating mode in the MJO initiation and propagation. *J. Geophys. Res. Atmos.*, **122**, 5837–5856, https://doi.org/10.1002/2016JD025665.

——, M. Minamide, R. G. Nystrom, X. Chen, S.-J. Lin, and L. M. Harris, 2019: Improving Harvey forecasts with next-generation weather satellites: Advanced hurricane analysis and prediction with assimilation of GOES-R all-sky radiances. *Bull. Amer. Meteor. Soc.*, **100**, 1217–1222, https://doi.org/10.1175/BAMS-D-18-0149.1.

Zhang, Y., F. Zhang, and D. J. Stensrud, 2018: Assimilating all-sky infrared radiances from *GOES-16* ABI using an ensemble Kalman filter for convection-allowing severe thunderstorms prediction. *Mon. Wea. Rev.*, **146**, 3363–3381, https://doi.org/10.1175/MWR-D-18-0062.1.

——, D. J. Stensrud, and F. Zhang, 2019: Simultaneous assimilation of radar and all-sky satellite infrared radiance observations for convection-allowing ensemble analysis and prediction of severe thunderstorms. *Mon. Wea. Rev.*, **147**, 4389–4409, https://doi.org/10.1175/MWR-D-19-0163.1.

——, ——, and E. E. Clothiaux, 2021: Benefits of the Advanced Baseline Imager (ABI) for ensemble-based analysis and prediction of severe thunderstorms. *Mon. Wea. Rev.*, **149**, 313–332, https://doi.org/10.1175/MWR-D-20-0254.1.

——, E. E. Clothiaux, and D. J. Stensrud, 2022: Correlation structures between satellite all-sky infrared brightness temperatures and the atmospheric state at storm scales. *Adv. Atmos. Sci.*, **39**, 714–732, https://doi.org/10.1007/s00376-021-0352-3.